Single-cell analysis of the human retina reveals stage-linked microglial states and neural-immune circuit rewiring in diabetic retinopathy

Luning Yang[1], Sen Lin[1], Yiwen Tao[1], Qi Pan[1], Tengda Cai[1], Yunyan Ye[2], Jianhui Liu[3], Yang Zhou[4], Quanyong Yi[5], Zen Huat Lu[6], Lie Chen[6], Gareth McKay[7], Richard Rankin[8], Yongqing Shao[5*], Weihua Meng[1*]

1 Nottingham Ningbo China Beacons of Excellence Research and Innovation Institute, University of Nottingham Ningbo China, Ningbo, China, 315100

2 Department of Ophthalmology, Lihuili Hospital affiliated with Ningbo University, Ningbo, China, 315040

3 Department of Cardiology, Lihuili Hospital affiliated with Ningbo University, Ningbo, China, 315040

4 Ningbo Institute of Innovation for Combined Medicine and Engineering, The Affiliated Li Huili Hospital, Ningbo University, Ningbo, China, 315201

5 Department of Ophthalmology, The Affiliated Ningbo Eye Hospital of Wenzhou Medical University, Ningbo, China, 315040

6 PAPRSB Institute of Health Sciences, Universiti Brunei Darussalam, Bandar Seri, Begawan, Brunei Darussalam, BE1410

7 Centre for Public Health, Institute of Clinical Science, Queen's University Belfast, Block B, Royal Hospital, Grosvenor Road, Belfast, UK, BT12 6BA

8 School of Mathematical Sciences, University of Nottingham Ningbo China, Ningbo, China, 315100

Corresponding Author:

Dr Weihua Meng

Address: Nottingham Ningbo China Beacons of Excellence Research and Innovation Institute, University of Nottingham Ningbo China, Ningbo, China, 315100. Tel: +86 574 88188632. Email: weihua.meng@nottingham.edu.cn. ORCID: 0000-0001-5388-8494

Dr Yongqing Shao

Address: Department of Ophthalmology, The Affiliated Ningbo Eye Hospital of Wenzhou Medical University, Ningbo, China, 315040. Tel: +86 15968412426. Email: sunniesyq@163.com. ORCID: 0009-0006-1319-8521

ORCID codes

Luning Yang: 0000-0001-9056-5950

Sen Lin: 0000-0002-7695-0964

Yiwen Tao: 0009-0000-0102-4205

Qi Pan: 0000-0003-0135-9122

Tengda Cai: 0000-0003-1617-506X

Yunyan Ye: 0009-0005-2325-1405

Jianhui Liu: 0009-0004-1341-0831

Yang Zhou: 0000-0001-9273-0489

Quanyong Yi: 0000-0002-9369-3998

Zen Huat Lu: 0000-0002-9408-0579

Lie Chen: 0000-0001-9764-4299

Gareth McKay: 0000-0001-8197-6280

Richard Rankin: 0000-0001-6445-2602

Yongqing Shao: 0009-0006-1319-8521

Weihua Meng: 0000-0001-5388-8494

Abstract

Diabetic retinopathy (DR) is a major cause of vision loss worldwide. Here, we conduct single-cell RNA sequencing of twenty human retina samples (from living and post-mortem donors) across non-diabetic, diabetic, and DR states to create a comprehensive transcriptomic atlas. We identify two stable microglial populations—homeostatic and inflammatory—that exist along a functional continuum, plus a neutrophil cluster within C1QA+ myeloid cells with dynamic transitions occurring throughout disease progression. Module-level analysis reveals divergent transcriptional trajectories: homeostatic microglia maintain energetic programs while selectively upregulating stress elements, whereas inflammatory microglia layer additional pro-inflammatory programs onto preserved biosynthetic foundations. Eleven co-expression modules organize into two major axes: an inflammatory-stress axis, and a regulatory/metabolic-motility axis, with a stable translation module persisting across disease stages. Cell communication analysis further highlights sophisticated neural-immune interactions, particularly between photoreceptors and microglia. Our findings provide insights into the complex cellular dynamics of DR progression and suggest potential therapeutic targets for early intervention.

Keywords: Single-cell RNA sequencing; Human retina; Diabetic retinopathy; Microglial states; Neural-immune interactions; Diabetes

Introduction

Diabetic retinopathy (DR) is the leading cause of vision impairment and blindness among working-age adults globally, posing a significant public health issue. It is characterized by progressive neurovascular dysfunction, involving both neurodegeneration and microvascular changes [1]. The global number of adults with diabetes has surpassed 800 million, with its prevalence rising from 7% to 14% between 1990 to 2020 [2]. Among them, 22.27% are affected by DR, and the global age-standardized prevalence of blindness caused by diabetic eye disease has increased by 14.9% over the same period [3, 4]. This trend poses a significant and growing burden on global health. While significant progress has been made in the treatment of DR, substantial limitations remain. Anti-VEGF therapy, panretinal photocoagulation, and corticosteroid treatments have demonstrated efficacy, but they are associated with incomplete responses, visual side effects, and complications [5, 6]. These therapies primarily target downstream effects rather than addressing the underlying pathogenic mechanisms [7].

The key gap in DR treatment is that current therapies focus on late-stage manifestations, with insufficient intervention in early molecular events. As a result, the complex cellular and molecular mechanisms driving disease progression are not adequately addressed [8]. Therefore, a comprehensive understanding of pathophysiology is needed to enable intervention in the early stages when the disease is more controllable. Targeted treatment at the cellular level, rather than addressing downstream complications, is crucial. This requires a deeper understanding of single-cell and molecular mechanisms [9].

While single-cell RNA sequencing (scRNA-seq) has emerged as a powerful tool for understanding complex biological systems, its application in DR research faces several critical limitations. The major challenge in the application of scRNA-seq in DR research is the difficulty in obtaining human retina

DR samples. While a few single-cell transcriptomic studies have generated retinal atlases, most published datasets utilize healthy donor eyes rather than samples from specific disease conditions, limiting our understanding of pathological states. To date, while several studies have examined retinal transcriptomes in animal models or healthy human retinas, single-cell analysis of complete human DR retina samples remains notably absent. Two recent studies focused on fibrovascular membranes, surgically harvested vitreous and peripheral blood from proliferative diabetic retinopathy (PDR) patients [10, 11], but neither fully recapitulates the complete pathogenesis of human DR as they focused on specific tissue types rather than the retina. Another challenge is the rapid post-mortem degradation of retinal tissue. In addition, the high cost of scRNA-seq and the difficulty in obtaining human retinal tissues hinder its large-scale application in DR and phased experimental design.

To investigate DR in retinal samples, more and more recent studies have focused on microglial cells, as these resident tissue macrophages play a pivotal role in initiating and exacerbating retinal inflammatory responses [12]. Our study aims to address these fundamental limitations by utilizing twenty human retinal samples spanning three disease stages, collected from both living donors and post-mortem specimens with minimal processing time to maximize transcriptional fidelity. We employed an integrated analytical approach combining cellular characterization, modular co-expression analysis, and intercellular communication mapping to comprehensively characterize the cellular and molecular features of DR progression.

Our integrated analysis reveals three critical insights that address fundamental gaps in the field. First, we demonstrate that retinal microglia exist along a functional continuum with two stable populations (homeostatic and inflammatory) that shift transcriptionally during DR progression through coordinated modular programs rather than wholesale phenotypic switching. Second, we uncover systematic

remodeling of intercellular communication networks, particularly the pathological shift from CD44-mediated to CXCR4-mediated MIF-CD74 signaling. Third, we validate the persistence of functionally distinct rod photoreceptor subtypes across disease stages [13], each engaging specialized signaling repertoires that differentially shape retinal immune dynamics. This study represents one of the first comprehensive single-cell analyses of human retina DR progression, revealing sophisticated neural-immune interactions that could advance our understanding of DR pathogenesis and open new avenues for targeted therapeutic interventions.

Materials and Methods

Human donor eyes collections for scRNA-seq analysis

From June 2023 to February 2025, we obtained twenty retina samples from non-diabetic, diabetic, and DR patients under protocols approved by the ethics committees of the University of Nottingham Ningbo China, the Lihuili Hospital, and the Ningbo Eye Hospital. Two samples of living donors were acquired through surgical enucleation at the Lihuili Hospital. The remaining eighteen samples came from the Ningbo Eye Hospital, comprising seven paired eyes and one single eye from deceased donors and three surgical specimens from enucleated patients. We utilized complete retinal specimens rather than selective punch biopsies, enabling comprehensive analysis of the entire retinal structure from center to periphery. In this study, 'fresh retinal samples' refers to two categories, the first is the living donor samples obtained during surgical enucleation and processed immediately within 10 min, and the second is post-mortem specimens processed within 6 h of death with strict temperature control without frozen. Table 1 provides detailed information on each sample.

Single-cell RNA sequencing

Human retina samples were dissociated for scRNA-seq using the LK003150-1bx Dissociation Kit (Worthington Biochemical Corporation) following the manufacturer's protocol. Tissue was placed on ice in a petri dish and manually cut into 2-4 mm pieces. After incubation in RPMI/enzyme mix (Miltenyi Biotec), the tissue fragments were transferred to a gentleMACS C tube for dissociation. After dissociation, the suspension was passed through a 70 µm cell strainer and centrifuged at 300 × g for 10 min at 4°C. The supernatant was removed, and 10 times volume of 1 x Red Blood Cell Lysis Solution (130-094-183, Miltenyi Biotec) were added to lyse red blood cells at 4°C for 10 min. Subsequently, 10 mL of 1x PBS containing 0.04% BSA was added to the suspension, which was then centrifuged again at 300 × g for 10 min. The suspension was mixed with AO/PI fluorescent dye (1:1 ratio) and incubated for 30 s, then cell viability was assessed for CountStar analysis. Viable cell suspension was resuspended in 1x PBS with 0.04% BSA to 700-1200 cells/µL (viability > 85%) for loading onto the 10x Genomics Chromium platform.

scRNA-seq libraries were made from 10,000 cells per sample using the Chromium Single Cell 3' Library and Gel Bead Kit (10X Genomics). 150 bp pair-ended sequencing was performed on Illumina Novaseq platform. Raw sequencing data quality was assessed using FastQC to ensure that (1) no more than three ambiguous "N" bases in total were present; (2) less than 20% of bases had a Phred quality score lower than 5; and (3) residue adapter sequences were removed. The resulting sequencing outputs were processed using the 10X Genomics Cell Ranger V8.0.1 pipeline with default settings. Transcript reads were aligned to the 10x Genomics Human reference index (GRCh38-2020-A). Each cell was assigned a unique, sample-specific identifier, and feature-barcode matrices were generated using the chromium cellular barcodes.

Quality control and doublets removal

For each sample, feature-barcode matrices were processed using the 10X Genomics Cell Ranger pipeline (https://www.10xgenomics.com/support/software/cell-ranger). We performed quality control and then doublet removal for each dataset to eliminate low-quality cells. Doublets were identified and removed using DoubletFinder (https://github.com/chris-mcginnis-ucsf/DoubletFinder). High-quality cells were selected based on the following criteria in the Seurat R package (v5.1.0) [14]: cells with a minimum gene count of 200, a UMI count greater than 400, and a mitochondrial read fraction of less than 20%. Cells passing these filters were retained for downstream analysis.

Data integration and clustering

After initial processing, the twenty datasets were integrated by Scanpy (v1.10.2) [15]. We used scVI-tools (v1.1.2) [16] to perform dimensionality reduction and batch-effect correction. A k-nearest neighbor (KNN) graph was built from the resulting latent space, and Leiden clustering was applied at multiple resolutions to identify and refine retinal cell types. Previously reported marker genes' expression of each cluster was used to annotate their corresponding retina cell type. This annotation workflow was further repeated to refine an accurate cell type annotation for the sub populations within each cell type. Sample bias introduced by the inclusion of fresh retinas from living donors was evaluated by analyzing the proportions of various cell types across all datasets.

Cell disturbance analysis

Transcriptomic variations across nonDM (samples without diabetes mellitus), DM (samples with diabetes mellitus), and DR (samples with diabetic retinopathy) conditions were assessed using Augur (v1.0.3) [17] and odds ratio (OR) analysis. To avoid instability from rare or small populations and non-ubiquitous clusters, T cells, retinal pigment epithelium, neutrophils, and retinal ganglion cells were excluded, and the comparison was restricted to nonDM versus DR. This pairwise comparison was

prioritized because Augur is designed for binary classification tasks and because nonDM versus DR exhibits the most pronounced transcriptomic remodeling, whereas DM exhibited minimal molecular alterations relative to nonDM. Augur calculated Area Under the Curve (AUC) scores to evaluate the predictive power of gene expression profiles for distinguishing nonDM from DR within each cell type, where higher AUC indicates stronger disease-associated perturbation. Label-permutation controls were performed to confirm that observed AUC values reflected true condition-expression associations rather than modeling artifacts. For compositional differences, we constructed a 2×2 contingency table with rows = that condition vs. all other conditions and columns = that cell type vs. all other cell types for each cell type and for each condition column (nonDM, DR), We computed the odds ratio and exact p value using Fisher's exact test, then applied Benjamini-Hochberg correction. OR > 1 denotes enrichment in the column's condition. This composition-aware metric complements Augur's separability, helping distinguish proportional shifts from transcriptional perturbations.

Differential expression and enrichment analysis

We performed differential expression (DE) to identify cell type or condition-specific markers using Seurat's FindAllMarkers and FindMarkers functions with an FDR < 0.05 and |log2FC| > 1 threshold for significance. To robustly define cluster-specific marker genes, particularly for microglial subpopulations, COSG (v0.9.0) [18] was applied following sub-clustering of C1QA-positive myeloid cells, which prioritizes genes with high specificity and robustness for each annotated cluster. Gene Ontology (GO) and Kyoto Encyclopedia of Genes and Genomes (KEGG) enrichment analysis were conducted by clusterProfiler (v4.10.1) [19]. Pathway scoring and enrichment were further evaluated by the irGSEA (v3.3.2) [20] framework, combining multiple methods (AUCell, UCell, singscore, ssgsea, JASMINE, viper) through robust rank aggregation (RRA).

Transcriptional pattern discovery

Microglia-specific gene co-expression modules were identified using Hotspot. First, Hotspot analysis (v1.1.1) identified spatially coordinated gene modules based on local correlation (https://github.com/YosefLab/Hotspot), leveraging dimensionality reduction and KNN graph construction. Module relationships were evaluated through correlation analysis, with scores calculated using UCell (v2.6.2) [21].

Cell communication analysis

CellChat (v1.6.1) was applied to perform cell-cell communication analysis [22]. First, CellChat objects were created for DR and nonDM conditions using the human CellChatDB database. Overexpressed genes and interactions were identified with default parameters and the analysis was enhanced by projecting data onto protein-protein interaction networks. Communication probabilities were computed using the triMean method. Signaling pathway analysis was performed by aggregating the communication probabilities of all ligand-receptor pairs associated with each pathway. To compare communication changes between nonDM and DR conditions, we specifically examined how each microglial subtype and rod photoreceptor subtype acted as signal senders or receivers with respect to other cell types

Results

Construction of the human retinal scRNA-seq atlas and lineages perturbed across DR

To investigate diabetic retinopathy progression, we performed scRNA-seq on twenty human retina samples encompassing three disease stages (nonDM, DM, DR). After stringent quality control and data integration using scVI, the retinal cell populations were visualized in a uniform manifold

approximation and projection (UMAP) plot (Figure 1A). Cells including cone, rod, bipolar (BC), amacrine (AC), horizontal (HC), retinal ganglion (RGC), Müller glia (MGC), astrocytes, microglia, T cells (TC), retinal pigment epithelium (RPE), and neutrophil, were identified according their significantly expressed distinctive marker genes (Figure 1B). Across donors, rods dominated in 19/20 samples, with group means markedly higher than any other lineage (nonDM 67.9 ± 18.1%, DM 56.5 ± 18.8%, DR 76.8 ± 6.3%; Table S1). For non-rod lineages, between-group differences were modest relative to within-group dispersion and showed substantial overlap. For example, MGC medians [IQR] were 10.8% [8.5–13.5%] in nonDM, 13.6% [13.3–30.5%] in DM, and 7.4% [6.2–9.9%] in DR; microglia were 1.8% [1.4–6.0%], 1.5% [0.4–2.6%], and 0.6% [0.5–0.7%], respectively. These distributions indicate notable inter-donor variability; accordingly, downstream analyses emphasize donor-level statistics and pair composition with within-lineage transcriptomic separability to distinguish proportional shifts from transcriptional perturbations. Then, we quantified disease-associated changes using a composition-aware metric (OR) and a perturbation-ranking approach (Augur) to explore a wider array of cell types associated with DR. To avoid instability from rare/small populations and a non-ubiquitous TC cluster, TC, RPE, Neutrophils, and RGCs were excluded, and the comparison was restricted to nonDM versus DR. Compositionally, the OR heatmap showed condition-specific enrichment among the remaining major lineages, for example, microglia were relatively enriched in nonDM, whereas cones appeared relatively enriched in DR (Figure 1C). In contrast, Augur prioritizes transcriptomic separability within each lineage, where higher AUC indicates stronger DR perturbation and permutation collapses values toward chance (≈0.5) (Figure 1D). The standard Augur run ranked HC highest (AUC = 0.682), followed by Cone (0.651), Microglia (0.649), Rod (0.625), and BC (0.593), with MGC, AST, and AC closest to chance. A label-permutation control

yielded AUCs near 0.5 for all types, supporting that the observed ordering reflects true label–expression structure rather than modeling artifacts (Figure 1E).

Retinal C1QA+ myeloid cells resolve into homeostatic and inflammatory microglia plus a neutrophil cluster

To further characterize microglial heterogeneity, we sub-clustered the major *C1QA*-positive population, comprising 7,352 cells. This analysis resolved three subpopulations: homeostatic microglia (MG-Homeostatic), inflammatory microglia (MG-Inflammatory), and neutrophils (Figure 2A). Quality control metrics supported genuine biological heterogeneity (Figure 2B): MG-Inflammatory exhibited higher transcriptional complexity (nFeature_RNA, nCount_RNA), neutrophils the lowest, and all clusters showed uniformly low mitochondrial gene percentages (percent.mt), indicating high viability. Cluster-defining signatures from COSG (Figure 2C, 2D) revealed MG-Homeostatic enrichment for core microglial markers (*C1QA*, *C1QB*) and ribosomal protein genes (e.g., *RPL14*, *RPS4X*), whereas MG-Inflammatory displayed an activated profile with upregulation of immune-related genes (e.g., *DOCK4*, *CD83*, *KLF6*). The third cluster was identified as neutrophils by canonical markers (*FCGR3B*, *S100A12*, *CXCR2*) with minimal microglial gene expression. All three populations were observed across non-DM, DM, and DR retinas from multiple donors, indicating that clustering was not driven by condition or batch (Figure 2E, Table S2).

Comprehensive differential expression further substantiated these cell identities (Table S3). After rigorously excising ribosomal and rod-photoreceptor genes, pathway enrichment on the MG-Homeostatic versus MG-Inflammatory contrast delineated two non-overlapping programs (Figure 3A, 3B): MG-Homeostatic was enriched for mitochondrial oxidative phosphorylation, aerobic respiration, proton transmembrane transport, and ATP metabolic processes, whereas MG-Inflammatory

was enriched for immune response–activating/regulating signaling, antigen processing and presentation of exogenous peptide antigen, macroautophagy, small GTPase–mediated signaling, endocytosis, lipid and atherosclerosis, osteoclast differentiation, and protein processing in the endoplasmic reticulum. irGSVA on immune hallmark gene sets (Figure 3C), while not excluding ribosomal/rod genes, recapitulated the same directional split across cell populations, strengthening the pathway-level separation between inflammatory and homeostatic programs; notably, neutrophils displayed a distinct immune-hallmark profile consistent with their canonical identity, providing orthogonal validation of all three populations. Importantly, homeostatic enrichment for oxidative phosphorylation and ATP metabolism persisted after removal of ribosomal and rod-photoreceptor genes and coincided with higher expression of antigen presentation/surveillance components (*CD74*, *HLA-DRA*/*DPA1*/*DPB1*, *TYROBP*, *AIF1*), arguing against a low-quality or degenerative state. Collectively, these pathway-level readouts from complementary methods indicate that inflammatory microglia engage coordinated cytokine and NF-κB/TLR-linked cascades, whereas homeostatic microglia maintain preserved bioenergetic tone alongside baseline immune surveillance functions.

Disease-stage dynamics of microglial subsets

Comparative analysis across disease states revealed distinct temporal activation patterns between the two microglial subsets (Figure 4). During early diabetic transition (DM vs. nonDM), MG-Homeostatic cells demonstrated functional stability with limited transcriptional changes, though notable upregulation of chemokines (*CCL2*, *CCL4*) and extracellular matrix remodeling genes (*FN1*) indicated early environmental sensing and low-grade inflammatory recruitment. Concurrently, transcriptional regulators (*NR4A2*) and neuroprotective factors (*CLU*) were enhanced, suggesting adaptive responses to hyperglycemic stress rather than overt activation. In

contrast, MG-Inflammatory cells entered a highly active state characterized by significant upregulation of pro-inflammatory mediators (*IL6*), chemokines (*CCL2, CXCL2/3*), matrix-receptor and vascular regulatory molecules (*FN1, STAB1, SDC3, VAV3*), and copper oxidase (*CP*). Notably, classical lysosomal proteases (*CTSL, CTSZ*) were upregulated while *CTSH* was downregulated, indicating reconfiguration of phagocytic-proteolytic networks. The absence of significant *IL1A*/*IL1B* and *TNF* elevation confirmed this stage as "regulatory activation" rather than full inflammatory amplification.

Disease progression to retinopathy (DR vs. DM) deepened this functional divergence. MG-Homeostatic cells exhibited predominantly broad transcriptional downregulation in DR relative to DM, with upregulation largely confined to ribosomal protein genes (*RPLP1, RPS23, RPL41*); accordingly, these cells showed no evident induction of classical pro-inflammatory or angiogenic markers, consistent with a chronic, low-grade reactive state and diminished functional activity. Conversely, MG-Inflammatory cells demonstrated an intensified inflammatory program in DR, with *IL1A* and *IL1B* upregulated, and a reconfigured chemokine network evidenced by marked *CCL2* downregulation, alongside reduced expression of other chemokines (*CXCL1, CXCL2, CXCL3*). Vascular-related molecular remodeling was also evident in MG-Inflammatory cells, highlighted by *PDGFB* upregulation and *NRP1* downregulation, suggesting an enhanced capacity for vascular regulatory interactions. Direct comparison of DR versus nonDM further validated this divergent activation model, demonstrating that retinal microglia employ complementary rather than uniform activation strategies as disease progresses.

Network-based analysis identifies microglial functional modules and disease-associated expression patterns

Gene co-expression analysis identified eleven discrete modules (M1-M11) with distinct molecular signatures (Figure 5A, Table S4). The correlation heatmap resolved two principal activation clusters: an inflammatory–stress cluster (M10, M4, M9) encompassing coordinated chemokine/cytokine, IL-1/immediate-early, and protein-stress programs; and a regulatory/metabolic–motility cluster (M5, M6, M8, M11) enriched for transcriptional control, lipid/metabolic genes, and remodeling/motility. M1 (ribosomal/translation) and M2 (rod-transcript signal) remained isolated; M2 is interpreted conservatively as photoreceptor carryover rather than a microglial program. M3 and M7 showed only moderate linkage to either cluster and were left ungrouped.

Consistent with this modular architecture, sample and donor level module scores (Figure 5B) showed that M1 was stable across nonDM, DM, and DR, with tightly clustered donor medians, indicating preserved baseline protein-synthesis capacity. In contrast, inflammatory–stress modules were higher in DR: M4 (IL1B with immediate-early TFs *JUN/FOS/EGR1/ATF3*), M10 (chemokines/cytokines *CCL3/CCL4/CXCL8/TNF*), and M9 (protein-stress/chaperones *HSPA1B/DNAJB1/HSPB1* and *DDIT4*) showed elevated scores in most DR donors. Distributions overlapped across groups and varied by donor, indicating heterogeneous activation. The DM group was generally intermediate/near baseline.

Rod photoreceptor subtype persistence in DR disease stages

Previous studies have identified functionally distinct rod photoreceptor subtypes, phototransduction-efficient rods (PER) specialized for light detection and mitochondrial ATP synthesis, and synaptic transmission-efficient rods (SER) enriched in neurotransmission processes. Unsupervised reclustering resolved three rod groups: Rod–SER-like (synaptic/adhesion program), Rod–PER-like (phototransduction/mitochondrial ETC–ATP program), and an intermediate mRod with mixed gene-expression patterns (Figure 5C). Group-specific enrichment and differential-expression analyses

aligned with previously reported PER/SER program (Figure 5D, 5E). MALAT1, which has been reported to decline with longer post-mortem intervals, ranked among the top differentially expressed transcripts between SER-like and PER-like groups. To assess potential source effects, we compared live and cadaver specimens and found that SER-like rods were more abundant in cadaver samples (overall mean 63.0% ± 10.9%) than in live samples (41.6% ± 21.2%), whereas PER-like rods were relatively higher in live samples (6.72% ± 7.30%) than in cadavers (3.51% ± 3.00%), indicating a retrieval-status bias in this cohort (Table S5). All three groups were detected across nonDM, DM, and DR, with inter-donor variability but no consistent stage-specific depletion.

Rod subtypes and microglial states engage distinct signaling repertoires consistent with their transcriptional programs in nonDM condition

In nonDM conditions, rod cell subtypes exhibit distinct communication profiles (Figure S1A-C). PER-like rods display a secreted-factor bias, with prominent MIF-CD74 to inflammatory microglia and VEGFB-FLT1 to glia, suggesting metabolic/vascular support, while contributing little to rod–rod adhesion. In contrast, SER-like rods are dominated by synaptic/adhesive signaling and show reduced MIF/VEGF output compared to PER-like rods and show NRG1-ERBB4 signaling to interneurons and astrocytes, consistent with neuron-glia crosstalk. The mRod population exhibits a hybrid/transition profile, carrying PER-like ECM/vascular axes (VEGFB, VTN, PSAP) together with SER-like synaptic/trophic axes (NRG1, NOTCH), indicating a transitional rather than distinct identity. Overall, PER-like rods act as cytokine/growth-factor emitters with limited physical contact, whereas SER-like rods prioritize structural connectivity and synaptic support, aligning with the PER/SER transcriptional dichotomy. For retinal C1QA+ myeloid subpopulations, MG-Homeostatic engage in maintenance-oriented signaling, sending SPP1 and participate in MIF and C3 signaling (Table S6).

MG-Inflammatory display an activated profile: they are the primary recipients of rod-derived MIF via CD74, and also take in TNF/TNFSF12, TGFβ1/2, ICAM1-β2-integrins, and extensive HLA-II-CD4 interactions. Neutrophils exhibit enriched chemotactic and adhesion signaling, consistent with their reactive characteristics.

Remodeling of Cell Communication from nonDM to DR

In DR, intercellular communication shifts markedly compared to non-diabetic controls (Table S7, Figure S2). The pro-inflammatory MIF–CD74 axis remains active but skews toward the CXCR4 co-receptor branch in DR, while the CD44-dependent branch is relatively diminished. Inflammatory microglia (CD74-expressing) are the chief recipients of MIF in both states, with photoreceptors—especially the PER-like rods—as prominent sources; notably, DR boosts MIF signaling via CD74+CXCR4 at the expense of the CD74+CD44 pathway. By contrast, the neuroprotective PSAP–GPR37 interactions collapse in DR: robust microglia-to-Müller glia and rod-to-glia PSAP signals evident in non-diabetic (nonDM) conditions are almost absent in DR. Likewise, several trophic/metabolic support axes decline. Vitronectin–integrin signaling from rods virtually disappears in DR, as do NAMPT–INSR (visfatin to insulin receptor) interactions and FGF1–FGFR1 signaling that were detectable in the healthy retina. On the myeloid side, microglial outgoing signals become more limited. While osteopontin (SPP1) signaling is substantially reduced rather than intensified, it remains a relatively prominent inflammatory output from microglia as other signals also wane.

Discussion

The advent of single-cell omics has significantly advanced our understanding of the pathological mechanisms underlying DR [9]. However, significant gaps persist, particularly in the absence of a comprehensive analysis of human DR retina samples. While animal models, including diabetic mice and non-human primates, have provided valuable insights [23-25], they fail to replicate the complexity of human DR pathogenesis due to species-specific differences. Recent efforts have partially addressed these gaps through single-cell analyses of human-derived tissues, such as PDR-fibrovascular membranes or blood mononuclear cells [26, 27]. However, the lack of studies involving human retina limits our ability to fully unravel the intricate cellular interactions and molecular mechanisms of DR in human.

To address this gap, we performed scRNA-seq on 20 human retinal samples covering three disease stages (nonDM, DM, and DR) from both surgical patients and donors. This comprehensive atlas spans all major retinal cell classes, including rod and cone photoreceptors, interneurons, Müller glia, vascular cells, and resident immune cells. In particular, the inclusion of microglia (resident immune cells known to mediate retinal inflammation [28, 29]) enables examination of their states across disease.

The molecular heterogeneity and functional dynamics of retinal microglia in DR are not fully understood due to insufficient comprehensive human retinal studies [28]. Traditionally described using the M1/M2 dichotomy, recent findings suggest that microglial activation spans a continuous spectrum rather than being defined by discrete phenotypes [28, 30]. Many studies that report “multiple microglial subpopulations” primarily reflect methodological advances that refine how putative groups are detected (e.g., deeper graph-based clustering, contrastive/representation learning, and improved batch correction) [31, 32]. Yet on low-dimensional visual embeddings, it often remains difficult to justify an additional, cleanly separable “third” cluster. In our dataset, we no longer find stable evidence for over two fully

independent microglial “states” based on scRNA-seq human retina tissues, even though our atlas comprising 20 samples. Within the C1QA+ myeloid population, we resolved three subpopulations: MG-Homeostatic microglia, MG-Inflammatory microglia, and a neutrophil cluster. MG-Homeostatic cells expressed core microglial markers and ribosomal protein genes, whereas MG-Inflammatory cells upregulated immune-activation genes. Pathway analysis showed that MG-Homeostatic cells were enriched for oxidative phosphorylation and metabolic processes, while MG-Inflammatory cells were enriched in cytokine/NF-κB and antigen-presentation pathways. These findings reveal that retinal myeloid cells span a spectrum from quiescent energy-maintaining states to pro-inflammatory activation. Comparison across disease stages revealed distinct dynamics for these subsets. During early diabetes, MG-Homeostatic cells remained largely stable, aside from modest upregulation of chemokines and stress regulators, suggesting an adaptive response to hyperglycemia. In contrast, MG-Inflammatory cells became highly active in the DM stage, upregulating pro-inflammatory mediators, chemokines, and matrix/vascular regulators. As DR developed, MG-Homeostatic cells showed broad downregulation of gene expression with no new inflammatory markers, reflecting a suppressed profile, whereas MG-Inflammatory cells further intensified their inflammatory program. The identification of homeostatic and inflammatory microglial subsets, while initially appearing to support a binary framework, actually reveals a more sophisticated biological reality when integrated with our disease-stage dynamics and co-expression network analyses.

The molecular architecture underlying this continuum becomes apparent through our modular analysis, which reveals how microglial activation operates through coordinated recruitment of distinct functional programs rather than wholesale phenotypic switching. The inflammatory-stress axis (encompassing IL-1β/immediate-early, chemokine/cytokine, and protein-stress modules) progressively accumulates

activity in DR while core biosynthetic machinery (translation module M1) remains remarkably stable across disease stages. This modular organization provides a mechanistic explanation for the observed divergent trajectories: homeostatic cells maintain their energetic backbone while selectively upregulating stress-response elements, whereas inflammatory cells layer additional pro-inflammatory programs onto this preserved foundation.

Moreover, our analysis confirms functionally distinct rod photoreceptor subtype populations persist consistently across the diabetes disease spectrum, with an additional intermediate mRod subtype displaying mixed transcriptional features. Crucially, these rod subtypes engage distinct communication repertoires that fundamentally shape retinal immune dynamics. PER-like rods function as primary secreted-factor emitters, prominently signaling through MIF-CD74 to inflammatory microglia and VEGFB-FLT1 to glial cells, while SER-like rods prioritize synaptic connectivity through NRG1-ERBB4 interactions with interneurons and astrocytes. This functional specialization becomes pathologically relevant in DR, where intercellular communication networks undergo systematic remodeling. Most significantly, the pro-inflammatory MIF-CD74 axis remains active but undergoes a critical qualitative shift toward CXCR4 co-receptor signaling in DR while CD44-mediated branches decline. This CD44 to CXCR4 transition reflects a shift from tissue-protective inflammation toward chronic, potentially tissue-damaging inflammatory signaling, as CXCR4 engagement typically promotes sustained inflammatory responses compared to the more regulatory CD44 pathway. Simultaneously, this inflammatory persistence occurs against a backdrop of collapsed neuroprotective networks. This coordination of maintained inflammatory signaling with lost homeostatic support reveals DR as fundamentally a disease of disrupted cellular cooperation, where specialized neuronal

subtypes shift from tissue-protective to tissue-damaging communication patterns while losing their capacity to maintain retinal homeostasis.

While our study provides insights into DR progression, we acknowledge several limitations. The relatively small sample size may limit statistical power for certain comparisons. However, this limitation reflects the challenges in acquiring human retina samples, especially from DR patients. The human retina is exceptionally rare and difficult to obtain due to several factors: (1) the limited availability of donor tissue meeting specific disease criteria, (2) the critical requirement for minimal post-mortem intervals to maintain RNA quality, and (3) the ethical and logistical complexities of collecting samples from living donors during surgery. Despite these constraints, our study represents one of the largest single-cell analyses of human retina in DR research to date. The inclusion of both living donor and post-mortem specimens with careful processing time control helps mitigate some limitations while maintaining data quality. Future studies with larger sample sizes would be valuable to validate our findings, though the inherent challenges of human retinal tissue collection will likely continue to pose significant barriers to large-scale analyses.

Statements and Declarations

Data availability

The single-cell RNA sequencing data generated in this study have been deposited in Figshare with the DOI: 10.6084/m9.figshare.28228949.

Author information

Authors and Affiliations

Nottingham Ningbo China Beacons of Excellence Research and Innovation Institute, University of Nottingham Ningbo China, Ningbo, China, 315100

Luning Yang, Sen Lin, Yiwen Tao, Qi Pan, Tengda Cai, Weihua Meng

Department of Ophthalmology, Lihuili Hospital affiliated with Ningbo University, Ningbo, China, 315040

Yunyan Ye

Department of Cardiology, Lihuili Hospital affiliated with Ningbo University, Ningbo, China, 315040

Jianhui Liu

Ningbo Institute of Innovation for Combined Medicine and Engineering, The Affiliated Li Huili Hospital, Ningbo University, Ningbo, China, 315201

Yang Zhou

Department of Ophthalmology, The Affiliated Ningbo Eye Hospital of Wenzhou Medical University, Ningbo, China, 315040

Quanyong Yi, Yongqing Shao

PAPRSB Institute of Health Sciences, Universiti Brunei Darussalam, Bandar Seri, Begawan, BE1410, Brunei Darussalam

Zen Huat Lu, Lie Chen

Centre for Public Health, Institute of Clinical Science, Queen's University Belfast, Block B, Royal Hospital, Grosvenor Road, Belfast, Northern Ireland, BT12 6BA

Gareth McKay

School of Mathematical Sciences, University of Nottingham Ningbo China, Ningbo, China, 315100

Richard Rankin

Authors' Contributions

LY drafted the paper and performed the analysis. SL, YT, QP, TC contributed to data formatting and correction. YY, JL, YZ, QY, ZL, LC, GM, and RR provided comments on the paper. YS, and WM organized the project and provided comments. Collaborators from Queen's University Belfast and Universiti Brunei Darussalam provided academic guidance and editorial suggestions only; they did not participate in data analysis, sample handling, or access to raw data. All substantive research activities were completed within Mainland China.

Acknowledgment

This study was mainly funded by the Pioneer and Leading Goose R&D Program of Zhejiang Province 2023 with reference number 2023C04049 and Ningbo International Collaboration Program 2023 with reference number 2023H025.

Corresponding authors

Correspondence to Dr. Weihua Meng and Dr. Yongqing Shao.

Consent to Publish

All authors have consent for publication.

Conflict of Interest

The authors have no conflicts of interest to disclose.

Ethics approval

This study was approved by the Ethics Committee of the University of Nottingham Ningbo China; The Lihuili Hospital affiliated with Ningbo University; The Affiliated Ningbo Eye Hospital of Wenzhou Medical University.

References

[1] L. Ji, H. Tian, K.A. Webster, W. Li, Neurovascular regulation in diabetic retinopathy and emerging therapies, Cellular and Molecular Life Sciences, 78 (2021) 5977-5985.

[2] B. Zhou, A.W. Rayner, E.W. Gregg, K.E. Sheffer, R.M. Carrillo-Larco, J.E. Bennett, J.E. Shaw, C.J. Paciorek, R.K. Singleton, A.B. Pires, Worldwide trends in diabetes prevalence and treatment from 1990 to 2022: a pooled analysis of 1108 population-representative studies with 141 million participants, The Lancet, 404 (2024) 2077-2093.

[3] Z.L. Teo, Y.-C. Tham, M. Yu, M.L. Chee, T.H. Rim, N. Cheung, M.M. Bikbov, Y.X. Wang, Y. Tang, Y. Lu, Global prevalence of diabetic retinopathy and projection of burden through 2045: systematic review and meta-analysis, Ophthalmology, 128 (2021) 1580-1591.

[4] J. Liu, H. Hu, S. Qiu, D. Wang, J. Liu, Z. Du, Z. Sun, The prevalence and risk factors of diabetic retinopathy: screening and prophylaxis project in 6 provinces of China, Diabetes, Metabolic Syndrome and Obesity: Targets and Therapy, (2022) 2911-2925.

[5] Y. Tomita, D. Lee, K. Tsubota, K. Negishi, T. Kurihara, Updates on the current treatments for diabetic retinopathy and possibility of future oral therapy, Journal of clinical medicine, 10 (2021) 4666.

[6] N. Cheung, I.Y. Wong, T.Y. Wong, Ocular anti-VEGF therapy for diabetic retinopathy: overview of clinical efficacy and evolving applications, Diabetes care, 37 (2014) 900-905.

[7] Q. Tang, F. Buonfiglio, E.W. Böhm, L. Zhang, N. Pfeiffer, C.A. Korb, A. Gericke, Diabetic Retinopathy: New Treatment Approaches Targeting Redox and Immune Mechanisms, Antioxidants, 13 (2024) 594.

[8] E.J. Duh, J.K. Sun, A.W. Stitt, Diabetic retinopathy: current understanding, mechanisms,

531 and treatment strategies, JCI insight, 2 (2017).

532 [9] X. Zhang, F. Zhang, X. Xu, Single-cell RNA sequencing in exploring the pathogenesis of

533 diabetic retinopathy, Clinical and Translational Medicine, 14 (2024) e1751.

534 [10] J. Wang, H. Sun, L. Mou, Y. Lu, Z. Wu, Z. Pu, M.-m. Yang, Unveiling the molecular

535 complexity of proliferative diabetic retinopathy through scRNA-seq, AlphaFold 2, and machine

536 learning, Frontiers in Endocrinology, 15 (2024) 1382896.

537 [11] R. Haliyur, D. Parkinson, J. Xu, Q. Li, Y. Huang, J. Liu, F. Ma, J. Gudjonsson, R. Rao,

538 Liquid biopsy for proliferative diabetic retinopathy: single-cell transcriptomics (scRNA-seq) of

539 human vitreous reveals inflammatory T cell signature, Investigative Ophthalmology & Visual

540 Science, 65 (2024) 935-935.

541 [12] Q. Hu, X. Zhang, H. Peng, J. Guan, Z. Huang, B. Jiang, D. Sun, A New Modulator of

542 Neuroinflammation in Diabetic Retinopathy: USP25, Inflammation, (2024) 1-16.

543 [13] L. Campello, M.J. Brooks, B.R. Fadl, H.S. Choi, S. Pal, A. Swaroop, Transcriptional

544 Heterogeneity and Differential Response of Rod Photoreceptor Pathway Uncovered by Single-

545 Cell RNA Sequencing of the Aging Mouse Retina, Aging Cell, e70001.

546 [14] Y. Hao, T. Stuart, M.H. Kowalski, S. Choudhary, P. Hoffman, A. Hartman, A. Srivastava, G.

547 Molla, S. Madad, C. Fernandez-Granda, Dictionary learning for integrative, multimodal and

548 scalable single-cell analysis, Nature biotechnology, 42 (2024) 293-304.

549 [15] F.A. Wolf, P. Angerer, F.J. Theis, SCANPY: large-scale single-cell gene expression data

550 analysis, Genome biology, 19 (2018) 1-5.

551 [16] A. Gayoso, R. Lopez, G. Xing, P. Boyeau, V. Valiollah Pour Amiri, J. Hong, K. Wu, M.

552 Jayasuriya, E. Mehlman, M. Langevin, A Python library for probabilistic analysis of single-cell

553 omics data, Nature biotechnology, 40 (2022) 163-166.

554 [17] M.A. Skinnider, J.W. Squair, C. Kathe, M.A. Anderson, M. Gautier, K.J. Matson, M. Milano,
555 T.H. Hutson, Q. Barraud, A.A. Phillips, Cell type prioritization in single-cell data, Nature
556 biotechnology, 39 (2021) 30-34.

557 [18] M. Dai, X. Pei, X.-J. Wang, Accurate and fast cell marker gene identification with COSG,
558 Briefings in bioinformatics, 23 (2022) bbab579.

559 [19] G. Yu, L.-G. Wang, Y. Han, Q.-Y. He, clusterProfiler: an R package for comparing
560 biological themes among gene clusters, Omics: a journal of integrative biology, 16 (2012)
561 284-287.

562 [20] C. Fan, F. Chen, Y. Chen, L. Huang, M. Wang, Y. Liu, Y. Wang, H. Guo, N. Zheng, Y. Liu,
563 irGSEA: the integration of single-cell rank-based gene set enrichment analysis, Briefings in
564 Bioinformatics, 25 (2024) bbae243.

565 [21] M. Andreatta, S.J. Carmona, UCell: Robust and scalable single-cell gene signature
566 scoring, Computational and structural biotechnology journal, 19 (2021) 3796-3798.

567 [22] S. Jin, M.V. Plikus, Q. Nie, CellChat for systematic analysis of cell–cell communication
568 from single-cell transcriptomics, Nature Protocols, (2024) 1-40.

569 [23] Y. Xiao, X. Hu, S. Fan, J. Zhong, X. Mo, X. Liu, Y. Hu, Single-cell transcriptome profiling
570 reveals the suppressive role of retinal neurons in microglia activation under diabetes mellitus,
571 Frontiers in Cell and Developmental Biology, 9 (2021) 680947.

572 [24] T. Niu, J. Fang, X. Shi, M. Zhao, X. Xing, Y. Wang, S. Zhu, K. Liu, Pathogenesis study
573 based on high-throughput single-cell sequencing analysis reveals novel transcriptional
574 landscape and heterogeneity of retinal cells in type 2 diabetic mice, Diabetes, 70 (2021)

575 1185-1197.

576 [25] I. Van Hove, L. De Groef, B. Boeckx, E. Modave, T.-T. Hu, K. Beets, I. Etienne, T. Van
577 Bergen, D. Lambrechts, L. Moons, Single-cell transcriptome analysis of the Akimba mouse
578 retina reveals cell-type-specific insights into the pathobiology of diabetic retinopathy,
579 Diabetologia, 63 (2020) 2235-2248.

580 [26] Z. Hu, X. Mao, M. Chen, X. Wu, T. Zhu, Y. Liu, Z. Zhang, W. Fan, P. Xie, S. Yuan,
581 Single-cell transcriptomics reveals novel role of microglia in fibrovascular membrane of
582 proliferative diabetic retinopathy, Diabetes, 71 (2022) 762-773.

583 [27] D. Liao, W. Fan, N. Li, R. Li, X. Wang, J. Liu, H. Wang, S. Hou, A single cell atlas of
584 circulating immune cells involved in diabetic retinopathy, Iscience, 27 (2024).

585 [28] Y. Wang, X. Yang, Y. Zhang, L. Hong, Z. Xie, W. Jiang, L. Chen, K. Xiong, S. Yang, M. Lin,
586 Single-cell RNA sequencing reveals roles of unique retinal microglia types in early diabetic
587 retinopathy, Diabetology & Metabolic Syndrome, 16 (2024) 49.

588 [29] T. Yuan, L. Dong, E.A. Pearsall, K. Zhou, R. Cheng, J.-X. Ma, The protective role of
589 microglial pparα in diabetic retinal neurodegeneration and neurovascular dysfunction, Cells,
590 11 (2022) 3869.

591 [30] A. Hu, M.H. Schmidt, N. Heinig, Microglia in retinal angiogenesis and diabetic retinopathy,
592 Angiogenesis, (2024) 1-21.

593 [31] E.G. O'Koren, C. Yu, M. Klingeborn, A.Y. Wong, C.L. Prigge, R. Mathew, J. Kalnitsky, R.A.
594 Msallam, A. Silvin, J.N. Kay, Microglial function is distinct in different anatomical locations
595 during retinal homeostasis and degeneration, Immunity, 50 (2019) 723-737. e727.

596 [32] B.M. Davis, M. Salinas-Navarro, M.F. Cordeiro, L. Moons, L. De Groef, Characterizing

597 microglia activation: a spatial statistics approach to maximize information extraction, Scientific

598 reports, 7 (2017) 1-12.

599
600

Figures

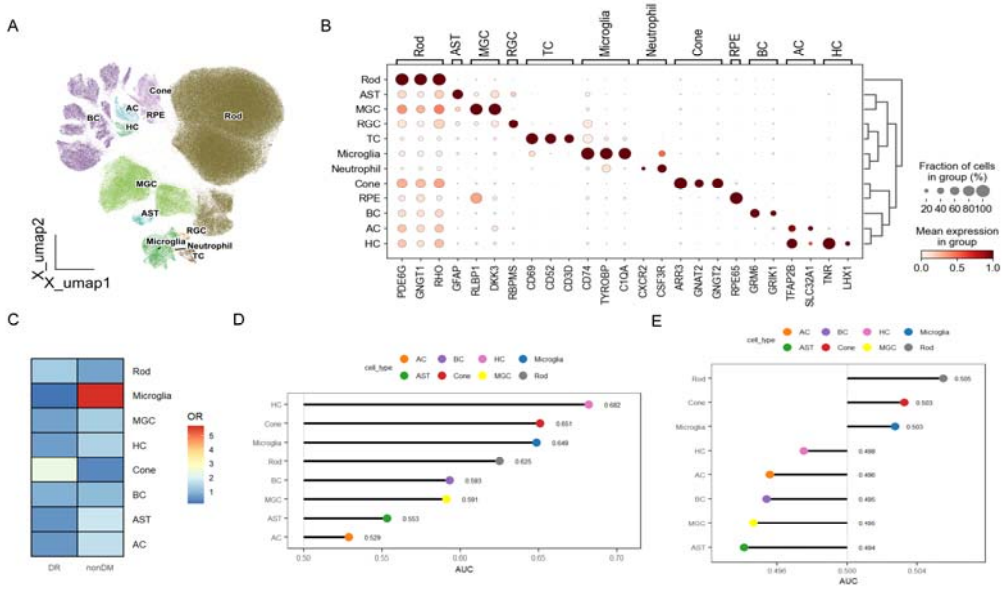

Figure1

(A) UMAP visualization of major retinal cell types identified from scRNA-seq data. Cell types are color-coded and labeled. BC: Bipolar cell, MGC: Müller glia cell, TC: T cell, AC: Amacrine cell, RGC: Retinal ganglion cell, HC: Horizontal cell, RPE: Retinal pigment epithelium, AST: Astrocytes.

(B) Dot plot of selected marker genes for major retinal cell types and T cells. Dot size represents the percentage of cells in each population expressing the gene, while color intensity indicates the normalized average expression level.

(C) Odds ratio (OR) heatmap showing compositional enrichment of cell types between non-diabetic (nonDM) and diabetic retinopathy (DR) conditions. Within each condition column, warmer colors indicate OR>1 (enrichment in that column's condition) and cooler colors indicate OR<1 (depletion).

(D) Augur analysis ranks retinal cell populations by their predictive accuracy (AUC) in distinguishing nonDM and DR samples. Higher AUC scores correspond to greater changes in population frequency during disease progression. Each dot represents a specific cell type, color-coded by identity.

(E) Label-permutation control for Augur. Randomizing condition labels yields **AUC ≈ 0.5** across cell classes, confirming that the separability observed in (D) reflects genuine condition–expression structure rather than model artifact.

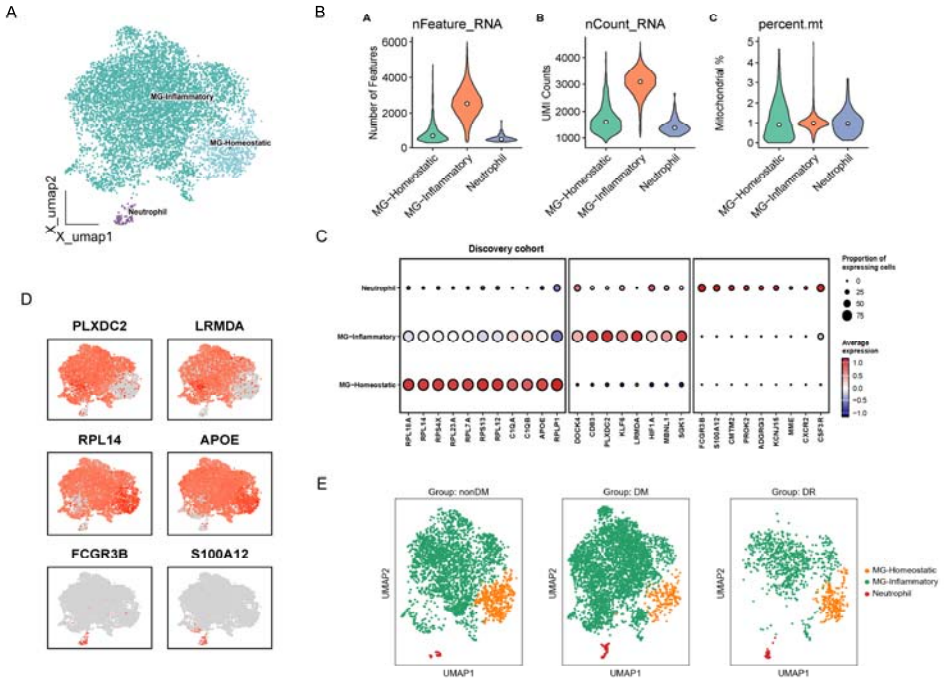

Figure 2

(A) UMAP visualization of C1QA+ myeloid cell subpopulation. Three distinct populations are labeled: MG-Homeostatic (homeostatic microglia), MG-Inflammatory (inflammatory microglia), and Neutrophil.

(B) Violin plots showing quality control metrics across the three myeloid subpopulations. Panel A displays the number of detected genes (nFeature_RNA), Panel B shows the total RNA count (nCount_RNA), and Panel C indicates the percentage of mitochondrial genes (percent.mt).

(C) Dot plot displaying cluster-defining marker genes identified by COSG across the discovery cohort. Dot size represents the proportion of cells expressing each gene within a population, while color

intensity indicates the normalized average expression level.

(D) Feature plots showing the spatial distribution of six representative marker genes on the UMAP.

(E) UMAP projections comparing the distribution of C1QA+ myeloid cell subpopulation across nonDM (non-diabetic), DM (diabetic), and DR (diabetic retinopathy) conditions.

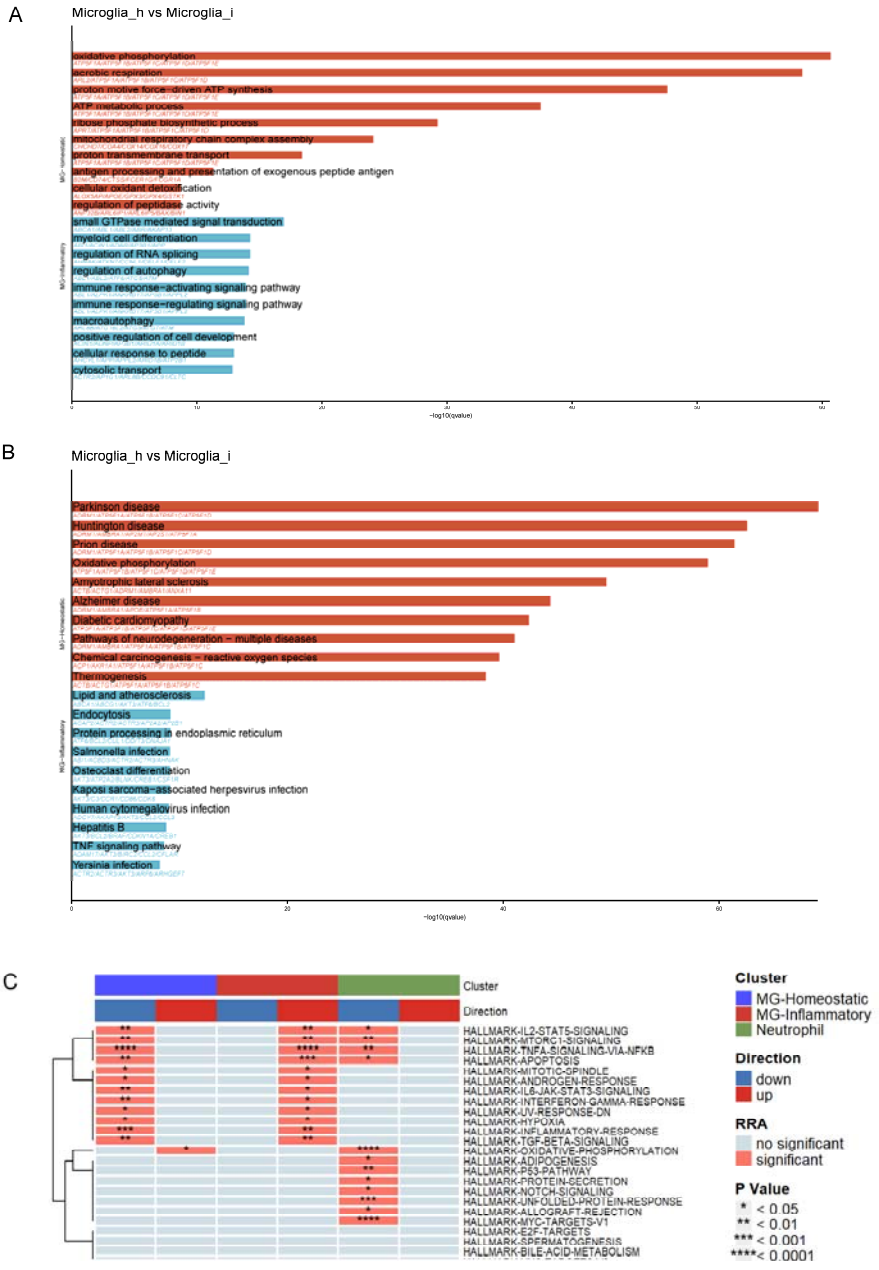

Figure 3

(A) Gene Ontology (GO) enrichment analysis showing significantly enriched biological processes between MG-Homeostatic (MG_h) and MG-Inflammatory (MG_i). Bar length represents -log10(adjusted p-value), with red bars indicating pathways enriched in MG-Homeostatic and blue bars showing pathways enriched in MG-Inflammatory.

(B) KEGG pathway enrichment analysis comparing MG-Homeostatic (MG_h) versus MG-Inflammatory (MG_i). Bar length represents -log10(adjusted p-value), with red bars indicating pathways enriched in MG-Homeostatic and blue bars showing pathways enriched in MG-Inflammatory.

(C) Heatmap of integrated gene set enrichment analysis (irGSEA) showing pathway activities across the three C1QA+ myeloid cell subpopulation. The top bar indicates cluster identity, and the second bar shows direction of regulation (blue: down, red: up). Significance levels are indicated by asterisks (* $p < 0.05$, ** $p < 0.01$, *** $p < 0.001$, **** $p < 0.0001$).

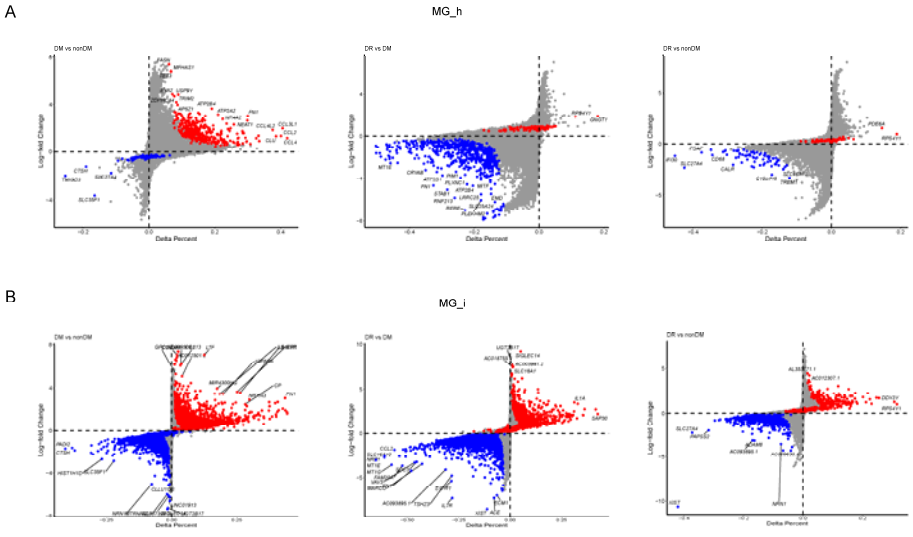

Figure 4

(A) Comparative differential gene expression analysis in MG-Homeostatic (MG_h) across disease

states using diagonal scatter plots. Left panel: DM (diabetic without retinopathy) versus nonDM (non-diabetic control); middle panel: DR (diabetic retinopathy) versus DM; right panel: DR versus nonDM. For all plots, the x-axis represents delta percentage of gene expression (difference in the proportion of cells expressing a gene between the two conditions), and the y-axis shows the log2 fold change (LogFC) in expression levels. Red points indicate significantly upregulated genes (LogFC > 0.25, adjusted p-value < 0.05) in the first mentioned condition, while blue points indicate significantly downregulated genes (LogFC < -0.25, adjusted p-value < 0.05) in the first mentioned condition. Key marker genes are labeled.

(B) Comparative differential gene expression analysis in MG-Inflammatory (MG_i) across disease states using diagonal scatter plots. Left panel: DM versus nonDM; middle panel: DR versus DM; right panel: DR versus nonDM. Axes and color coding follow the same convention as panel A.

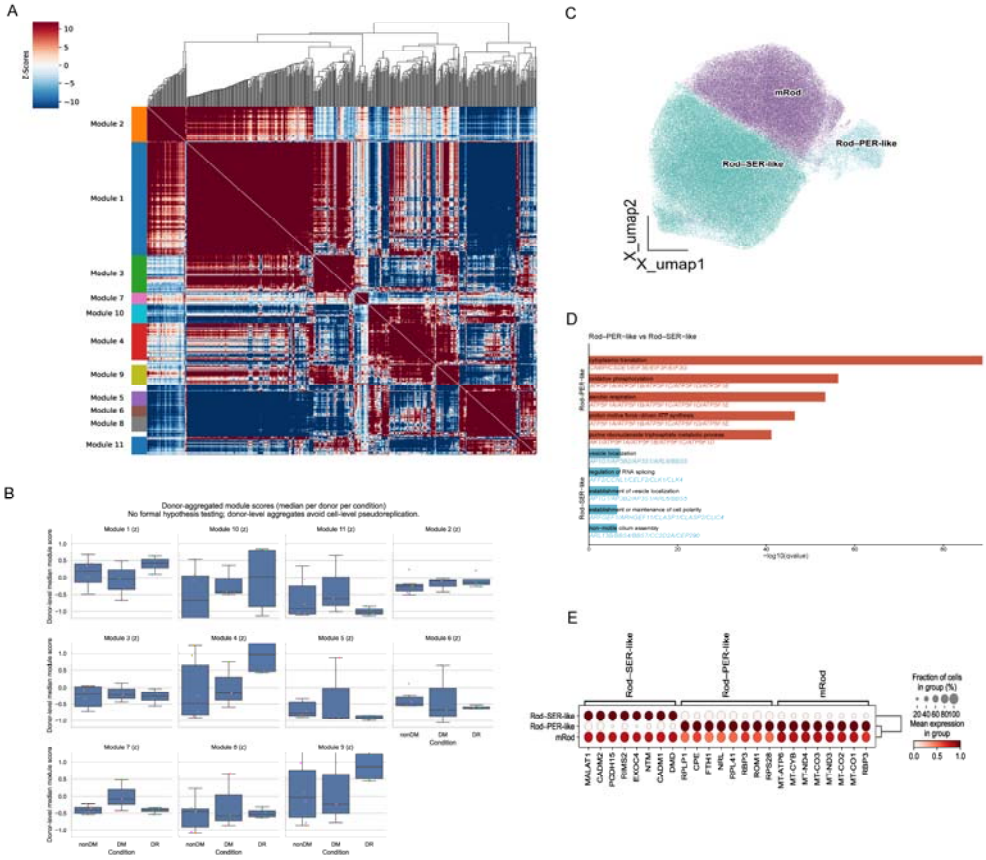

Figure 5

(A) Correlation heatmap showing relationships between identified Hotspot modules. Sidebar colors represent different module classifications. Color scale indicates correlation strength (red: positive correlation, blue: negative correlation)

(B) Donor-aggregated module scores (median per donor per condition) across disease stages (nonDM: non-diabetic control, DM: diabetic without retinopathy, DR: diabetic retinopathy) for representative modules.

(C) UMAP visualization of rod photoreceptor subclusters identified. Three functionally distinct rod subpopulations are resolved: Rod-SER-like (synaptic transmission-efficient rods with synaptic/adhesion program), Rod-PER-like (phototransduction-efficient rods with

phototransduction/mitochondrial ETC/ATP program), and mRod (intermediate subtype with mixed gene-expression patterns).

(D) Gene Ontology (GO) enrichment analysis comparing Rod-PER-like versus Rod-SER-like photoreceptors. Bar length represents -log10(adjusted p-value), with red bars indicating pathways enriched in Rod-PER-like and blue bars showing pathways enriched in Rod-SER-like.

(E)) Dot plot of selected marker genes for rod subtypes. Dot size represents the percentage of cells in each population expressing the gene, while color intensity indicates the normalized average expression level.

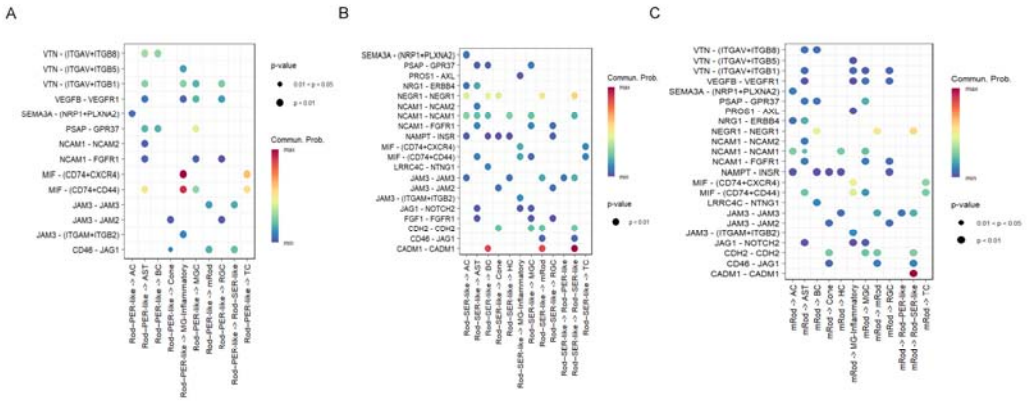

Figure S1

(A–C) Dot plots of sender-specific interactions inferred by CellChat, shown separately for Rod-PER-like (A), Rod-SER-like (B), and mRod (C) subtypes as senders toward the indicated receiver cell classes (x-axis). The y-axis lists selected ligand-receptor pairs highlighted in the Results. Color encodes CellChat communication probability (higher = stronger inferred interaction), and dot size encodes significance (larger dots: $P < 0.01$; smaller dots: $0.01 \leq P < 0.05$).

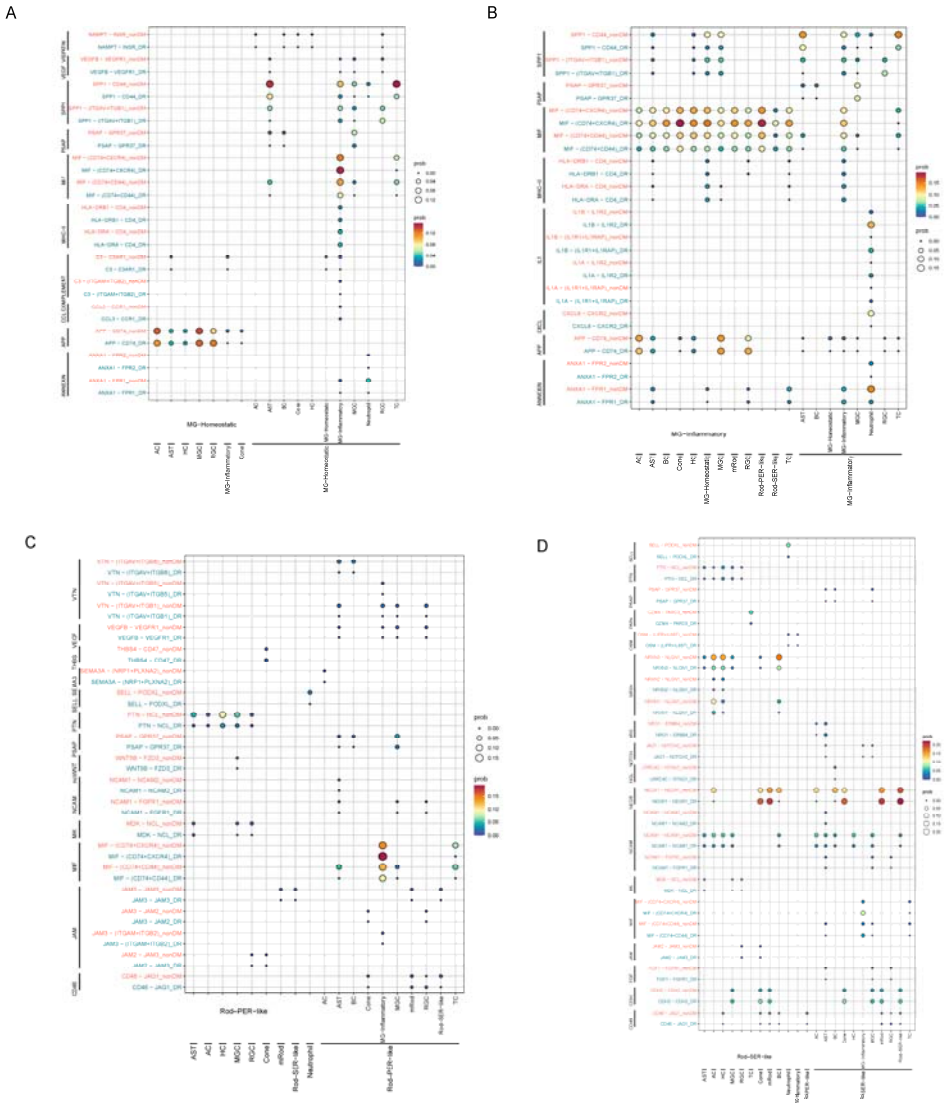

Figure S2

(A-D) Dot plots of both sender and receiver interactions inferred by CellChat, shown separately for MG-Homeostatic (homeostatic microglia) (A), MG-Inflammatory (inflammatory microglia) (B), Rod-PER-like (phototransduction-efficient rods) (C), and Rod-SER-like (synaptic transmission-efficient rods) (D). The y-axis lists selected ligand-receptor pairs, while the x-axis shows the interacting cell types as either senders (left sections) or receivers (right sections). Color encodes CellChat communication probability (orange/red = higher probability indicating stronger inferred interaction; blue = lower probability), and dot size encodes significance (larger dots: $P < 0.01$; smaller dots: $0.01 \leq P < 0.05$).

TableS1 Donor information and retinal cell composition of twenty samples in this study. This table provides detailed information about the donors, including donor ID, other disease status, eye condition, sex, age, diabetic status, and reason for eye removal or death. Additionally, it includes the proportions and counts of major retinal cell types for each retina sample.

TableS2 Composition and abundance of C1QA+ myeloid cell subpopulations across human retinal samples. This table summarizes the cellular composition of C1QA+ myeloid populations identified through sub-clustering analysis across 20 human retinal samples spanning three disease stages. Three distinct subpopulations were resolved: microglia-homeostatic (MG-Homeostatic), microglia-homeostatic (MG-Homeostatic), and neutrophils.

TableS3 Differential expression between microglia-homeostatic (MG-Homeostatic) and microglia-homeostatic (MG-Homeostatic) with ribosomal and rod-photoreceptor genes excluded. This table presents comprehensive differential expression analysis comparing MG-Homeostatic versus MG-Inflammatory microglia subsets identified from C1QA+ myeloid cell subclustering across 20 human retinal samples. To ensure identification of core microglia-intrinsic differences, ribosomal protein genes and rod-photoreceptor transcripts were rigorously excluded from the analysis to prevent technical artifacts from abundant contaminant signals.

TableS4 Gene co-expression modules identified in retinal microglia cells.

TableS5 Rod photoreceptor subtype composition across human retinal samples. This table presents the distribution of three rod photoreceptor subtypes identified through subclustering analysis across 20 human retinal samples. Recent studies have identified functionally distinct rod subtypes, phototransduction-efficient rods (PER-like) and synaptic transmission-efficient rods (SER-like), and

our analysis confirms these populations persist consistently across the diabetes disease spectrum, with an additional intermediate mRod subtype.

TableS6 Intercellular communication interactions involving retinal immune cells in non-diabetic group. This table presents significant cell-cell communication interactions identified through CellChat analysis, focusing on signaling pathways involving retinal myeloid cell populations (microglia-homeostatic, microglia-inflammatory, neutrophils) alongside their interactions with other retinal cell types.

TableS7 Disease-stage comparison of intercellular signaling interactions. This table presents comprehensive cell-cell communication analysis comparing nonDM (non-diabetic) and DR (diabetic retinopathy) conditions, revealing systematic remodeling of retinal intercellular signaling networks during disease progression.

Table 1. Retinal sample information

Sample	Donor ID	Tissue Source	Eye	Sex	Age(y)	Diabetic Status*	Eye Removal/Death Reason	Hospital†
1	D1	Live	Left	Male	76	DM	Corneal staphyloma	L.H.
2	D2	Live	Left	Male	55	nonDM	Phthisis bulbi	L.H.
3	D3	Live	Right	Male	71	nonDM	Corneal ulcer	Y.H.
4	D4	Live	Left	Female	50	nonDM	Phthisis bulbi	Y.H.
5	D5	Live	Right	Female	68	nonDM	Corneal perforation	Y.H.
6	D6	Cadaver	Left	Male	34	nonDM	Cerebral hemorrhage	Y.H.
7	D7	Cadaver	Left	Female	92	nonDM	Natural death	Y.H.
8	D7	Cadaver	Right	Female	92	nonDM	Natural death	Y.H.
9	D8	Cadaver	Left	Female	55	DM	Traumatic brain injury	Y.H.
10	D8	Cadaver	Right	Female	55	DM	Traumatic brain injury	Y.H.
11	D9	Cadaver	Left	Male	55	DR	Brainstem hemorrhage	Y.H.
12	D9	Cadaver	Right	Male	55	DR	Brainstem hemorrhage	Y.H.
13	D10	Cadaver	Left	Male	35	DR	Traumatic shock	Y.H.
14	D10	Cadaver	Right	Male	35	DR	Traumatic shock	Y.H.
15	D11	Cadaver	Left	Male	84	DR	Prostate cancer	Y.H.
16	D11	Cadaver	Right	Male	84	DR	Prostate cancer	Y.H.
17	D12	Cadaver	Left	Male	69	DR	Lung cancer	Y.H.
18	D12	Cadaver	Right	Male	69	DR	Lung cancer	Y.H.
19	D13	Cadaver	Left	Female	87	DM	Liver cancer	Y.H.
20	D13	Cadaver	Right	Female	87	DM	Liver cancer	Y.H.

*DM, diabetes mellitus without diabetic retinopathy DR; diabetic retinopathy; nonDM, non-diabetic retinopathy nor diabetic. Because the tissues were obtained intra-operatively or post-mortem and detailed fundus imaging records were unavailable, the exact stage or subtype of diabetic retinopathy (e.g., NPDR vs PDR) could not be ascertained for the DR cases.

†L.H., The Ningbo Lihuili Hospital; Y.H., The Ningbo Eye Hospital.

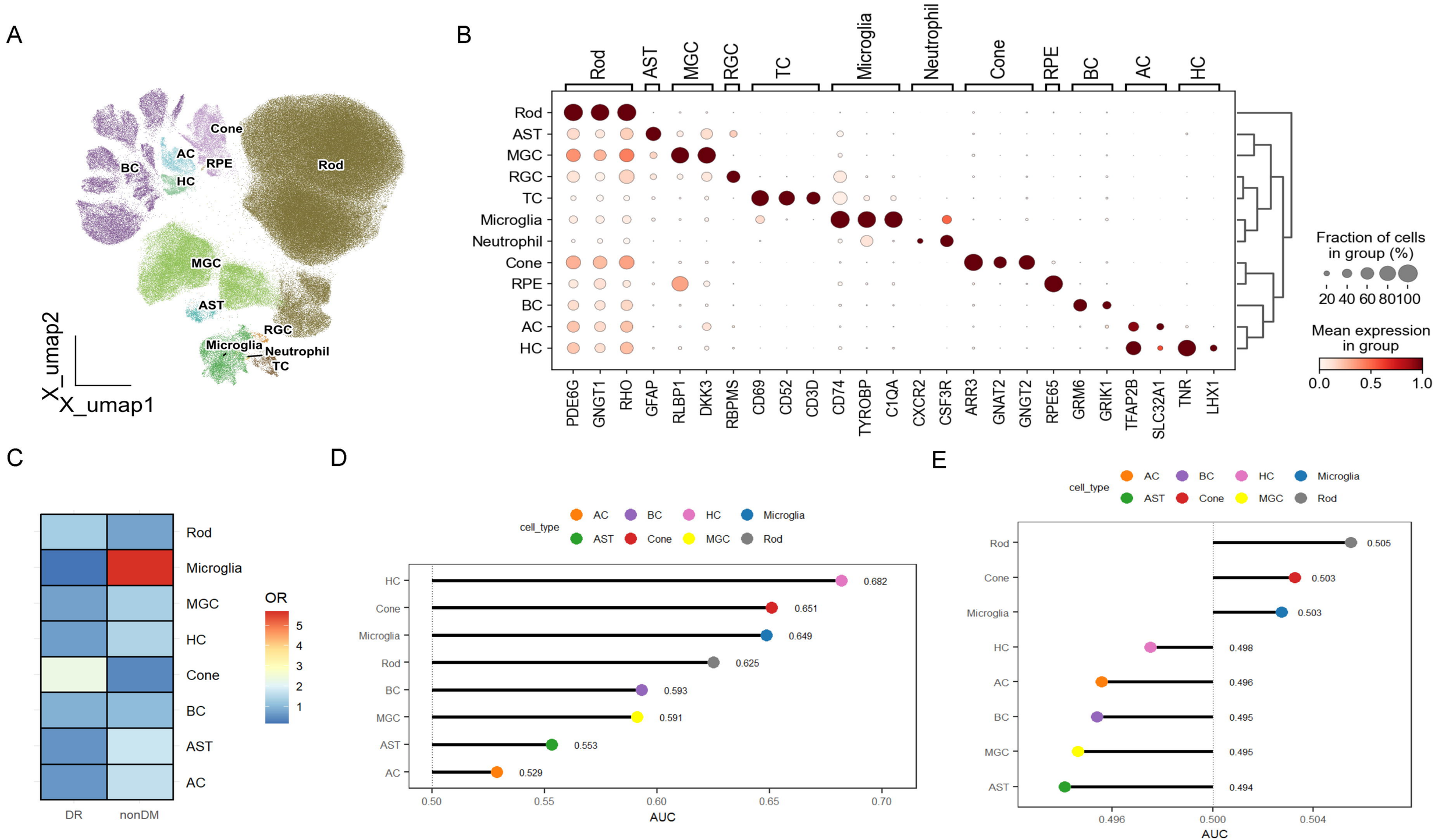
A
Cone
AC
RPE
BC
HC
Rod
MGC
AST
RGC
Microglia
Neutrophil
TC
X_umap2
X_umap1
B
Rod
AST
MGC
RGC
TC
Microglia
Neutrophil
Cone
RPE
BC
AC
HC
PDE6G
GNGT1
RHO
GFAP
RLBP1
DKK3
RBPMS
CD69
CD52
CD3D
CD74
TYROBP
C1QA
CXCR2
CSF3R
ARR3
GNAT2
GNGT2
RPE65
GRM6
GRIK1
TFAP2B
SLC32A1
TNR
LHX1
Fraction of cells in group (%)
20 40 60 80100
Mean expression in group
0.0 0.5 1.0
C
Rod
Microglia
MGC
HC
Cone
BC
AST
AC
DR
nonDM
OR
5
4
3
2
1
D
cell_type
AC BC HC Microglia
AST Cone MGC Rod
HC 0.682
Cone 0.651
Microglia 0.649
Rod 0.625
BC 0.593
MGC 0.591
AST 0.553
AC 0.529
0.50 0.55 0.60 0.65 0.70
AUC
E
cell_type
AC BC HC Microglia
AST Cone MGC Rod
Rod 0.505
Cone 0.503
Microglia 0.503
HC 0.498
AC 0.496
BC 0.495
MGC 0.495
AST 0.494
0.496 0.500 0.504
AUC

A

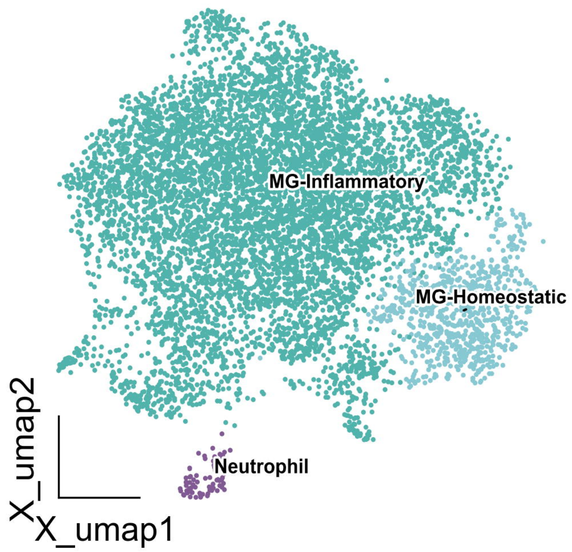
MG-Inflammatory
MG-Homeostatic
Neutrophil
X_umap2
X_umap1

B

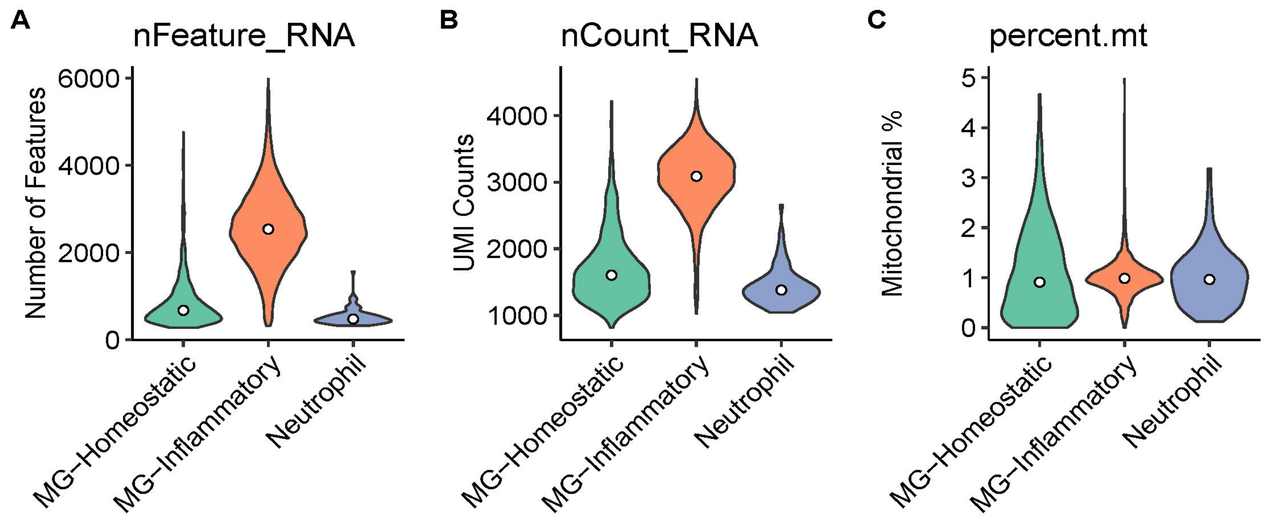
A
nFeature_RNA
Number of Features
6000
4000
2000
0
B
nCount_RNA
UMI Counts
4000
3000
2000
1000
C
percent.mt
Mitochondrial %
5
4
3
2
1
0
MG−Homeostatic
MG−Inflammatory
Neutrophil

C

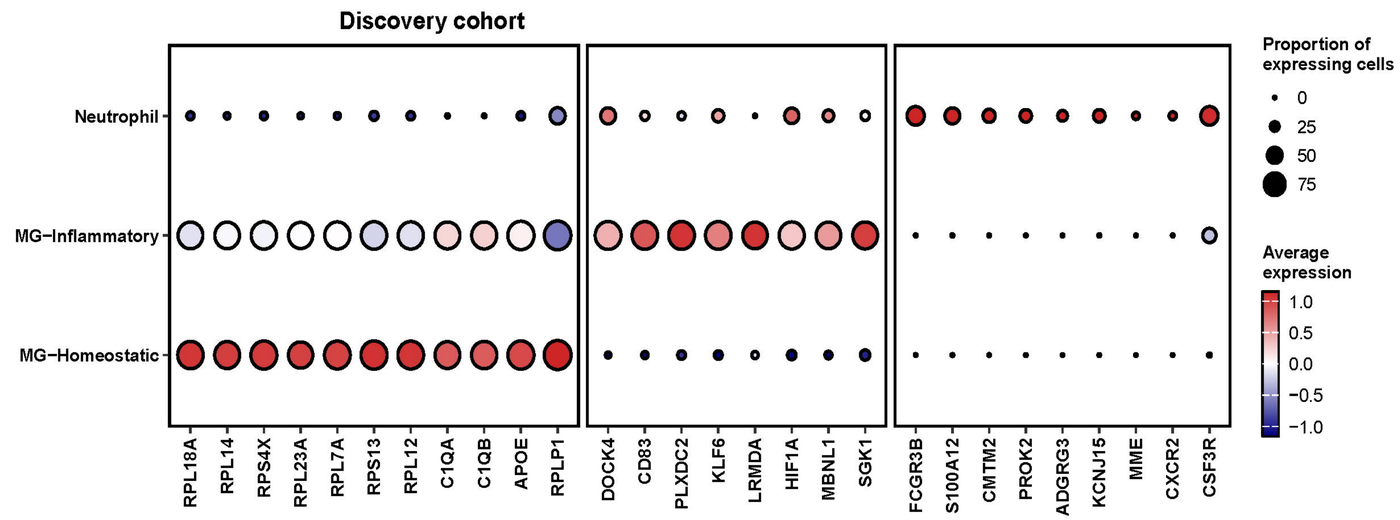
Discovery cohort
Neutrophil
MG−Inflammatory
MG−Homeostatic
RPL18A
RPL14
RPS4X
RPL23A
RPL7A
RPS13
RPL12
C1QA
C1QB
APOE
RPLP1
DOCK4
CD83
PLXDC2
KLF6
LRMDA
HIF1A
MBNL1
SGK1
FCGR3B
S100A12
CMTM2
PROK2
ADGRG3
KCNJ15
MME
CXCR2
CSF3R
Proportion of expressing cells
0
25
50
75
Average expression
1.0
0.5
0.0
−0.5
−1.0

D

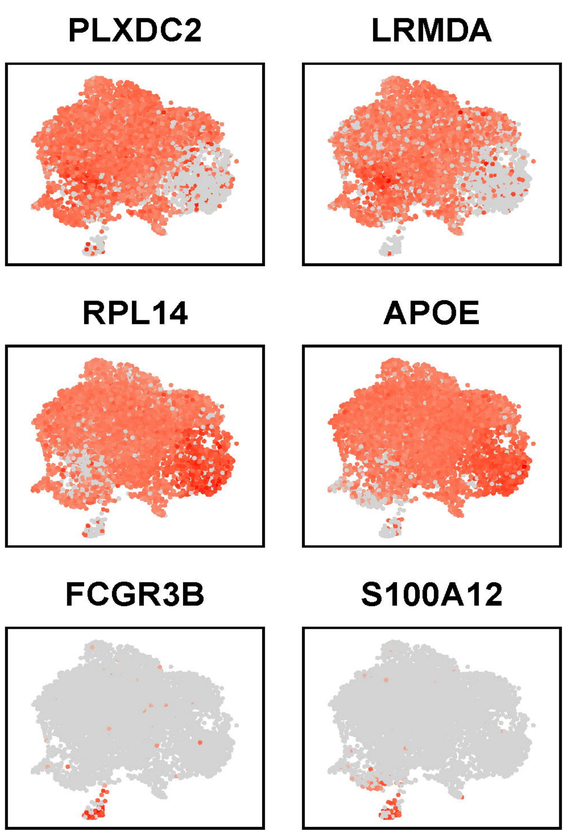
PLXDC2
LRMDA
RPL14
APOE
FCGR3B
S100A12

E

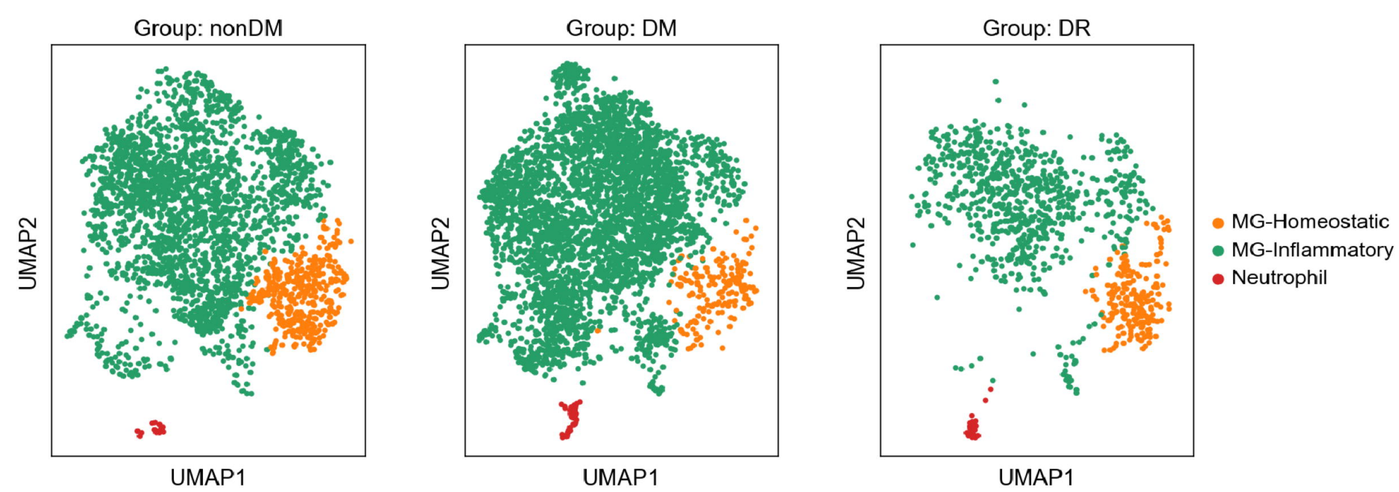
Group: nonDM
Group: DM
Group: DR
UMAP2
UMAP1
MG-Homeostatic
MG-Inflammatory
Neutrophil

A

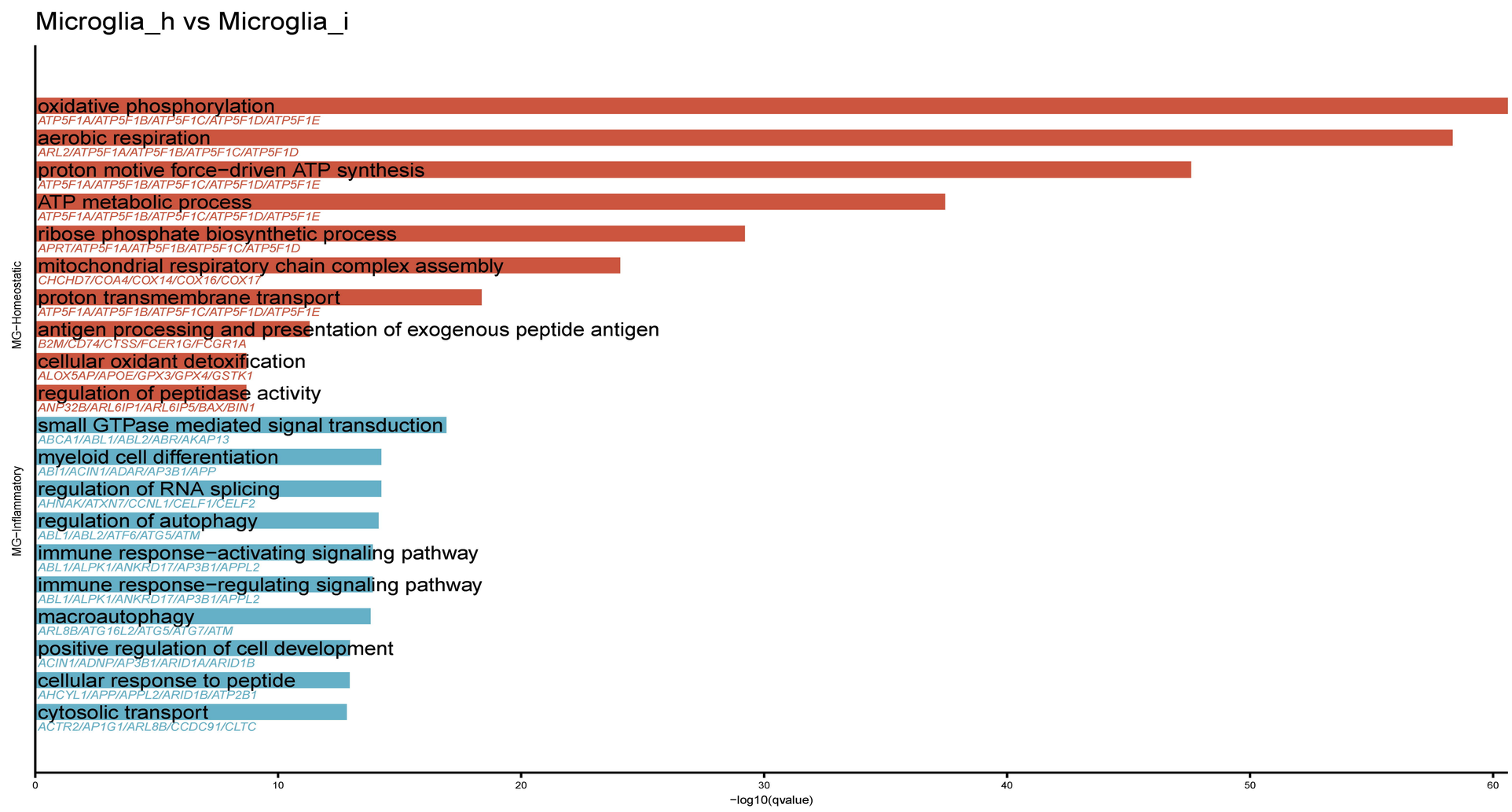
Microglia_h vs Microglia_i
MG−Homeostatic
MG−Inflammatory
oxidative phosphorylation
ATP5F1A/ATP5F1B/ATP5F1C/ATP5F1D/ATP5F1E
aerobic respiration
ARL2/ATP5F1A/ATP5F1B/ATP5F1C/ATP5F1D
proton motive force−driven ATP synthesis
ATP5F1A/ATP5F1B/ATP5F1C/ATP5F1D/ATP5F1E
ATP metabolic process
ATP5F1A/ATP5F1B/ATP5F1C/ATP5F1D/ATP5F1E
ribose phosphate biosynthetic process
APRT/ATP5F1A/ATP5F1B/ATP5F1C/ATP5F1D
mitochondrial respiratory chain complex assembly
CHCHD7/COA4/COX14/COX16/COX17
proton transmembrane transport
ATP5F1A/ATP5F1B/ATP5F1C/ATP5F1D/ATP5F1E
antigen processing and presentation of exogenous peptide antigen
B2M/CD74/CTSS/FCER1G/FCGR1A
cellular oxidant detoxification
ALOX5AP/APOE/GPX3/GPX4/GSTK1
regulation of peptidase activity
ANP32B/ARL6IP1/ARL6IP5/BAX/BIN1
small GTPase mediated signal transduction
ABCA1/ABL1/ABL2/ABR/AKAP13
myeloid cell differentiation
ABI1/ACIN1/ADAR/AP3B1/APP
regulation of RNA splicing
AHNAK/ATXN7/CCNL1/CELF1/CELF2
regulation of autophagy
ABL1/ABL2/ATF6/ATG5/ATM
immune response−activating signaling pathway
ABL1/ALPK1/ANKRD17/AP3B1/APPL2
immune response−regulating signaling pathway
ABL1/ALPK1/ANKRD17/AP3B1/APPL2
macroautophagy
ARL8B/ATG16L2/ATG5/ATG7/ATM
positive regulation of cell development
ACIN1/ADNP/AP3B1/ARID1A/ARID1B
cellular response to peptide
AHCYL1/APP/APPL2/ARID1B/ATP2B1
cytosolic transport
ACTR2/AP1G1/ARL8B/CCDC91/CLTC
0
10
20
30
40
50
60
−log10(qvalue)

B

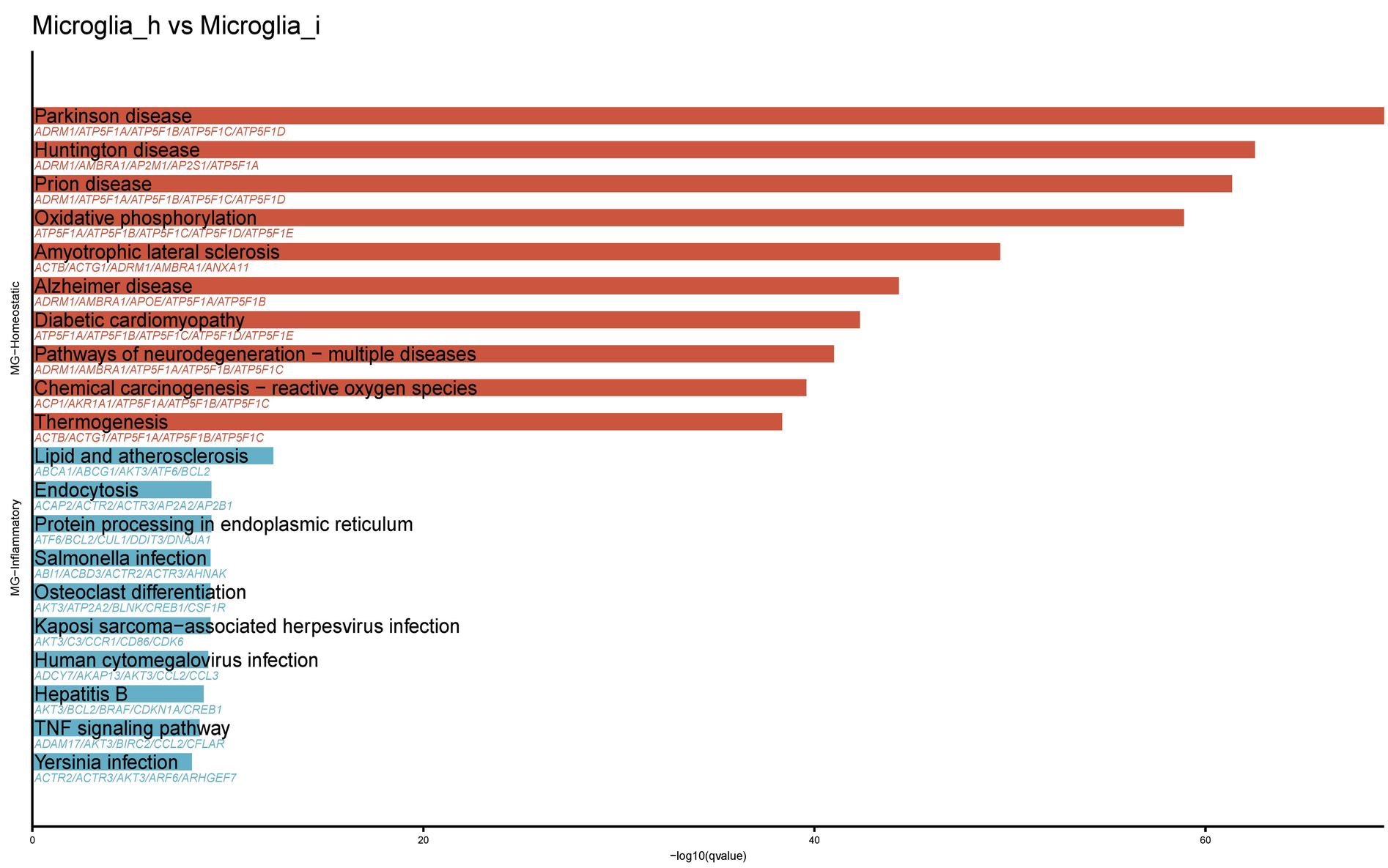
Microglia_h vs Microglia_i
MG−Homeostatic
MG−Inflammatory
Parkinson disease
ADRM1/ATP5F1A/ATP5F1B/ATP5F1C/ATP5F1D
Huntington disease
ADRM1/AMBRA1/AP2M1/AP2S1/ATP5F1A
Prion disease
ADRM1/ATP5F1A/ATP5F1B/ATP5F1C/ATP5F1D
Oxidative phosphorylation
ATP5F1A/ATP5F1B/ATP5F1C/ATP5F1D/ATP5F1E
Amyotrophic lateral sclerosis
ACTB/ACTG1/ADRM1/AMBRA1/ANXA11
Alzheimer disease
ADRM1/AMBRA1/APOE/ATP5F1A/ATP5F1B
Diabetic cardiomyopathy
ATP5F1A/ATP5F1B/ATP5F1C/ATP5F1D/ATP5F1E
Pathways of neurodegeneration − multiple diseases
ADRM1/AMBRA1/ATP5F1A/ATP5F1B/ATP5F1C
Chemical carcinogenesis − reactive oxygen species
ACP1/AKR1A1/ATP5F1A/ATP5F1B/ATP5F1C
Thermogenesis
ACTB/ACTG1/ATP5F1A/ATP5F1B/ATP5F1C
Lipid and atherosclerosis
ABCA1/ABCG1/AKT3/ATF6/BCL2
Endocytosis
ACAP2/ACTR2/ACTR3/AP2A2/AP2B1
Protein processing in endoplasmic reticulum
ATF6/BCL2/CUL1/DDIT3/DNAJA1
Salmonella infection
ABI1/ACBD3/ACTR2/ACTR3/AHNAK
Osteoclast differentiation
AKT3/ATP2A2/BLNK/CREB1/CSF1R
Kaposi sarcoma−associated herpesvirus infection
AKT3/C3/CCR1/CD86/CDK6
Human cytomegalovirus infection
ADCY7/AKAP13/AKT3/CCL2/CCL3
Hepatitis B
AKT3/BCL2/BRAF/CDKN1A/CREB1
TNF signaling pathway
ADAM17/AKT3/BIRC2/CCL2/CFLAR
Yersinia infection
ACTR2/ACTR3/AKT3/ARF6/ARHGEF7
0
20
40
60
−log10(qvalue)

C

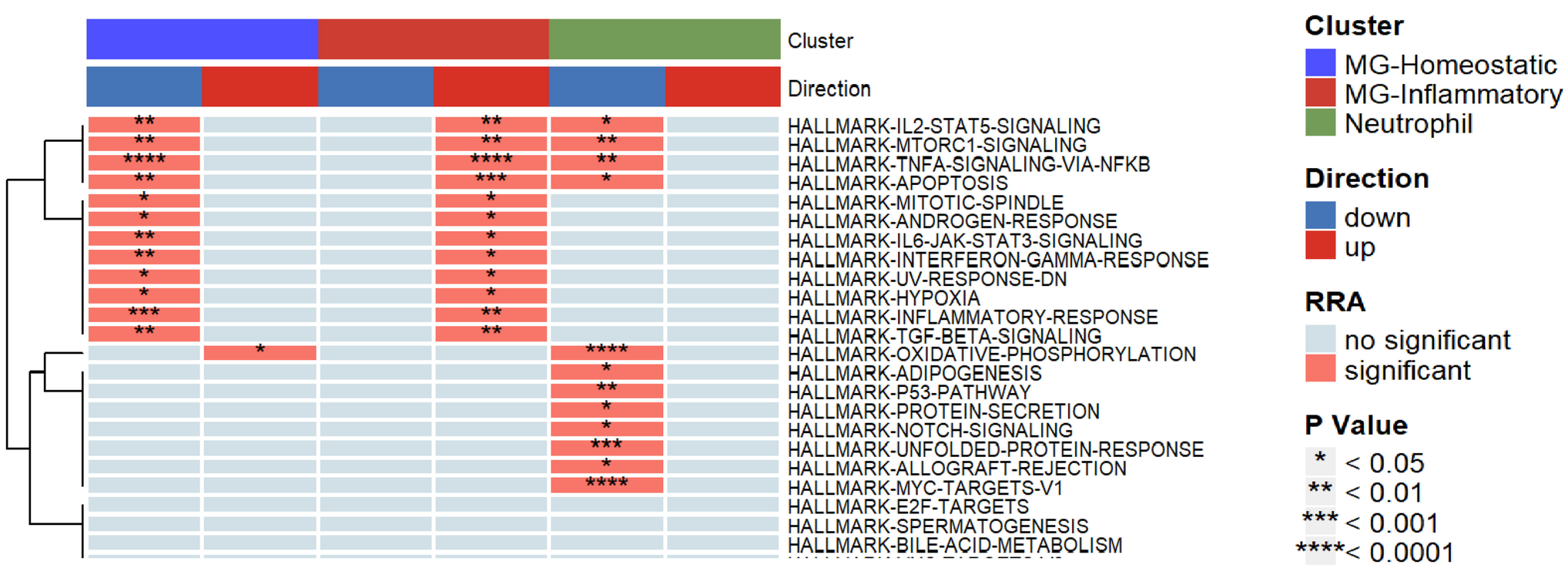
Cluster
Direction
HALLMARK-IL2-STAT5-SIGNALING
HALLMARK-MTORC1-SIGNALING
HALLMARK-TNFA-SIGNALING-VIA-NFKB
HALLMARK-APOPTOSIS
HALLMARK-MITOTIC-SPINDLE
HALLMARK-ANDROGEN-RESPONSE
HALLMARK-IL6-JAK-STAT3-SIGNALING
HALLMARK-INTERFERON-GAMMA-RESPONSE
HALLMARK-UV-RESPONSE-DN
HALLMARK-HYPOXIA
HALLMARK-INFLAMMATORY-RESPONSE
HALLMARK-TGF-BETA-SIGNALING
HALLMARK-OXIDATIVE-PHOSPHORYLATION
HALLMARK-ADIPOGENESIS
HALLMARK-P53-PATHWAY
HALLMARK-PROTEIN-SECRETION
HALLMARK-NOTCH-SIGNALING
HALLMARK-UNFOLDED-PROTEIN-RESPONSE
HALLMARK-ALLOGRAFT-REJECTION
HALLMARK-MYC-TARGETS-V1
HALLMARK-E2F-TARGETS
HALLMARK-SPERMATOGENESIS
HALLMARK-BILE-ACID-METABOLISM
Cluster
MG-Homeostatic
MG-Inflammatory
Neutrophil
Direction
down
up
RRA
no significant
significant
P Value
* < 0.05
** < 0.01
*** < 0.001
**** < 0.0001

A

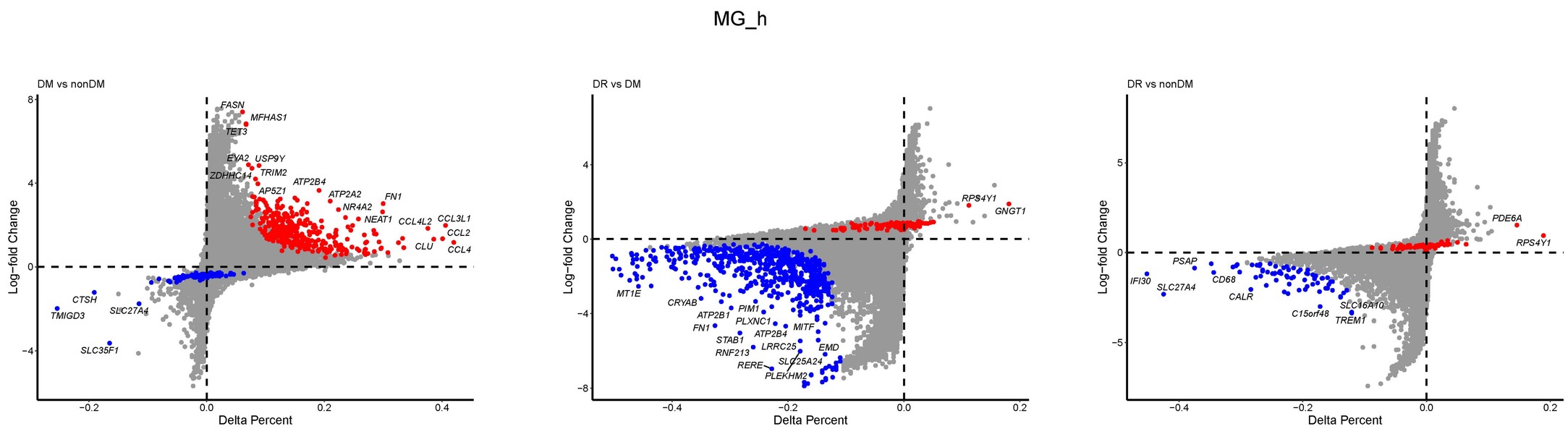
MG_h
DM vs nonDM
DR vs DM
DR vs nonDM
Log−fold Change
Delta Percent
FASN
MFHAS1
TET3
EYA2
USP9Y
ZDHHC14
TRIM2
ATP2B4
AP5Z1
ATP2A2
FN1
NR4A2
NEAT1
CCL4L2
CCL3L1
CCL2
CLU
CCL4
CTSH
TMIGD3
SLC27A4
SLC35F1
RPS4Y1
GNGT1
MT1E
CRYAB
ATP2B1
PIM1
PLXNC1
FN1
ATP2B4
MITF
STAB1
LRRC25
EMD
RNF213
SLC25A24
RERE
PLEKHM2
PDE6A
PSAP
IFI30
CD68
CALR
C15orf48
SLC16A10
TREM1

B

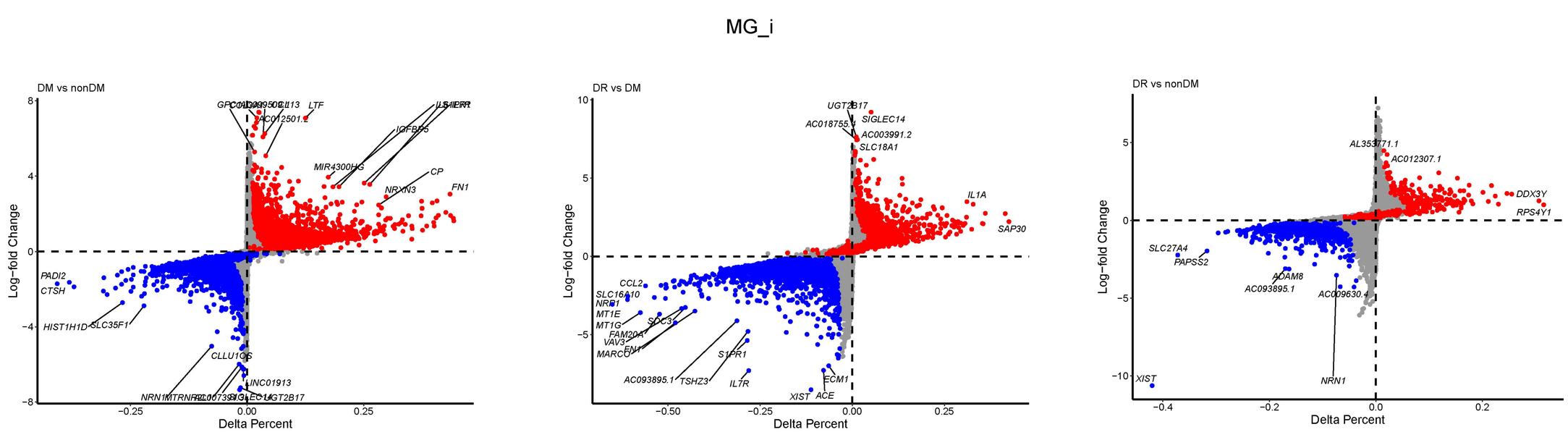
MG_i
DM vs nonDM
DR vs DM
DR vs nonDM
Log−fold Change
Delta Percent
LTF
IGFBP5
MIR4300HG
CP
NRXN3
FN1
PADI2
CTSH
HIST1H1D
SLC35F1
CLLU1OS
LINC01913
UGT2B17
UGT2B17
SIGLEC14
AC018755.1
AC003991.2
SLC18A1
IL1A
SAP30
CCL2
SLC16A10
NRN1
MT1E
MT1G
SDC3
FAM20A
VAV3
MARCO
FN1
S1PR1
AC093895.1
TSHZ3
IL7R
XIST
ACE
ECM1
AL353771.1
AC012307.1
DDX3Y
RPS4Y1
SLC27A4
PAPSS2
ADAM8
AC093895.1
AC009630.4
XIST
NRN1

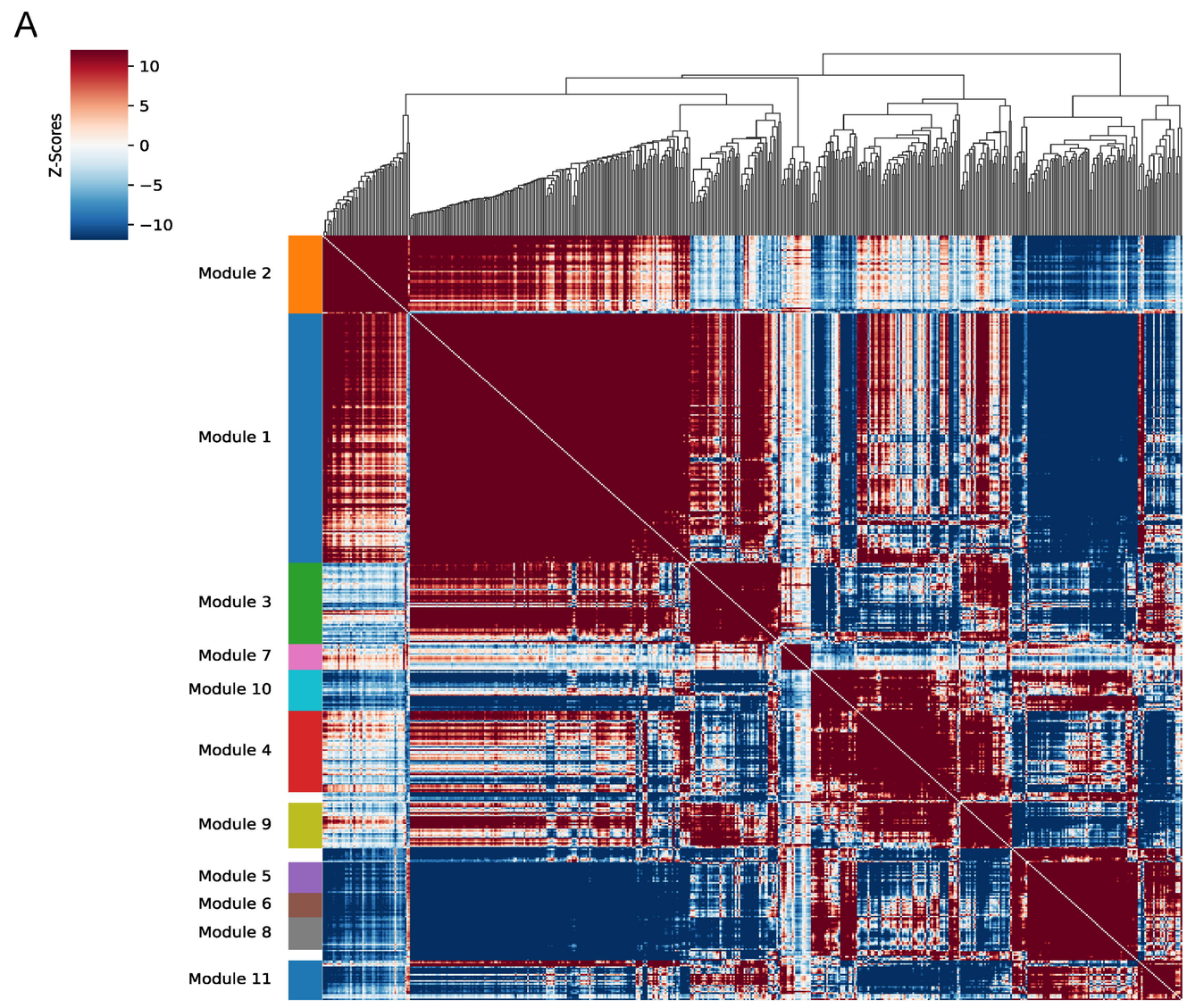
A
Z-Scores
10
5
0
−5
−10
Module 2
Module 1
Module 3
Module 7
Module 10
Module 4
Module 9
Module 5
Module 6
Module 8
Module 11

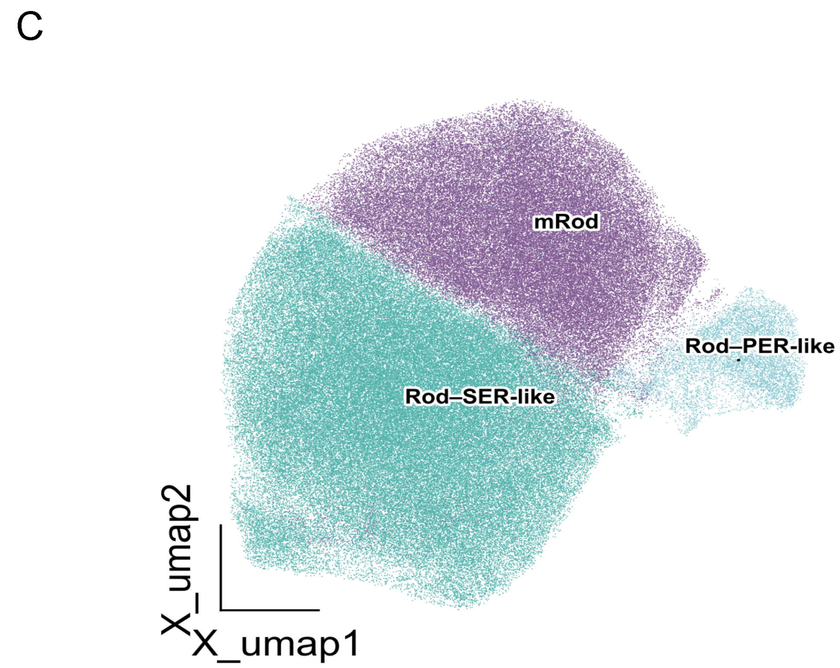
C
mRod
Rod–PER-like
Rod–SER-like
X_umap2
X_umap1

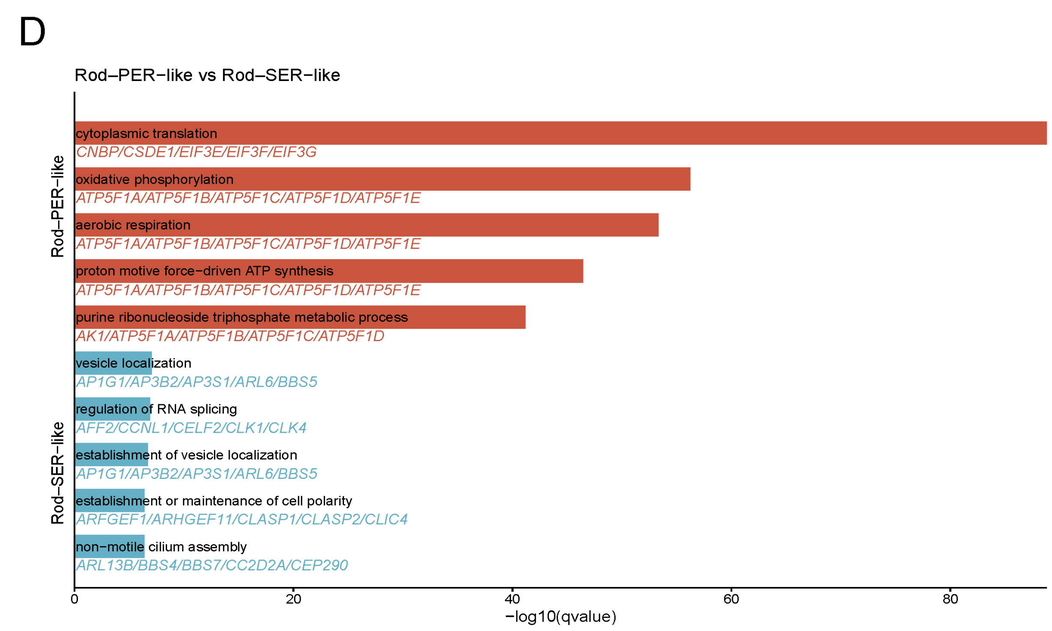
D
Rod–PER−like vs Rod–SER−like
Rod–PER−like
Rod–SER−like
cytoplasmic translation
CNBP/CSDE1/EIF3E/EIF3F/EIF3G
oxidative phosphorylation
ATP5F1A/ATP5F1B/ATP5F1C/ATP5F1D/ATP5F1E
aerobic respiration
ATP5F1A/ATP5F1B/ATP5F1C/ATP5F1D/ATP5F1E
proton motive force−driven ATP synthesis
ATP5F1A/ATP5F1B/ATP5F1C/ATP5F1D/ATP5F1E
purine ribonucleoside triphosphate metabolic process
AK1/ATP5F1A/ATP5F1B/ATP5F1C/ATP5F1D
vesicle localization
AP1G1/AP3B2/AP3S1/ARL6/BBS5
regulation of RNA splicing
AFF2/CCNL1/CELF2/CLK1/CLK4
establishment of vesicle localization
AP1G1/AP3B2/AP3S1/ARL6/BBS5
establishment or maintenance of cell polarity
ARFGEF1/ARHGEF11/CLASP1/CLASP2/CLIC4
non−motile cilium assembly
ARL13B/BBS4/BBS7/CC2D2A/CEP290
0
20
40
60
80
−log10(qvalue)

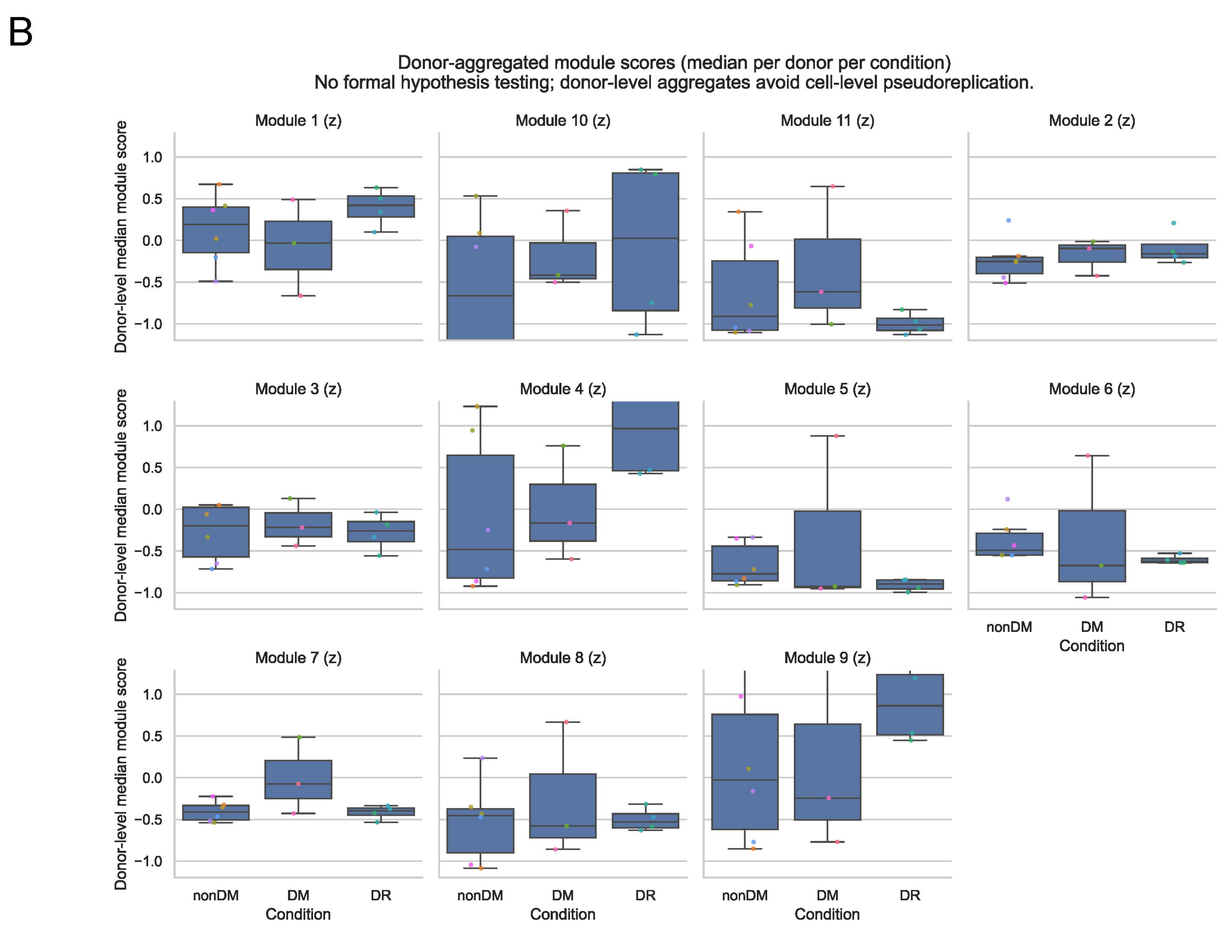
B
Donor-aggregated module scores (median per donor per condition)
No formal hypothesis testing; donor-level aggregates avoid cell-level pseudoreplication.
Module 1 (z)
Module 10 (z)
Module 11 (z)
Module 2 (z)
Module 3 (z)
Module 4 (z)
Module 5 (z)
Module 6 (z)
Module 7 (z)
Module 8 (z)
Module 9 (z)
Donor-level median module score
1.0
0.5
0.0
−0.5
−1.0
nonDM
DM
DR
Condition

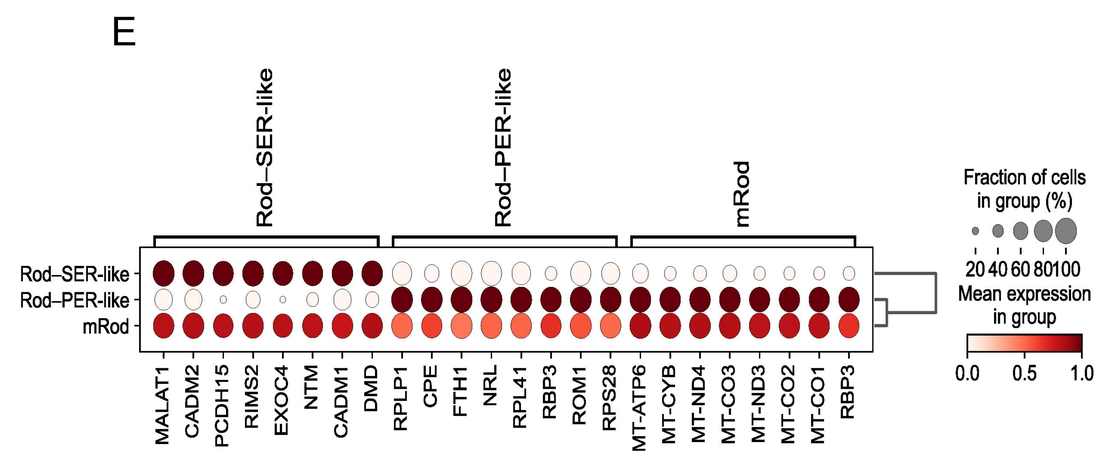
E
Rod–SER-like
Rod–PER-like
mRod
Rod–SER-like
Rod–PER-like
mRod
MALAT1
CADM2
PCDH15
RIMS2
EXOC4
NTM
CADM1
DMD
RPLP1
CPE
FTH1
NRL
RPL41
RBP3
ROM1
RPS28
MT-ATP6
MT-CYB
MT-ND4
MT-CO3
MT-ND3
MT-CO2
MT-CO1
RBP3
Fraction of cells in group (%)
20 40 60 80 100
Mean expression in group
0.0
0.5
1.0

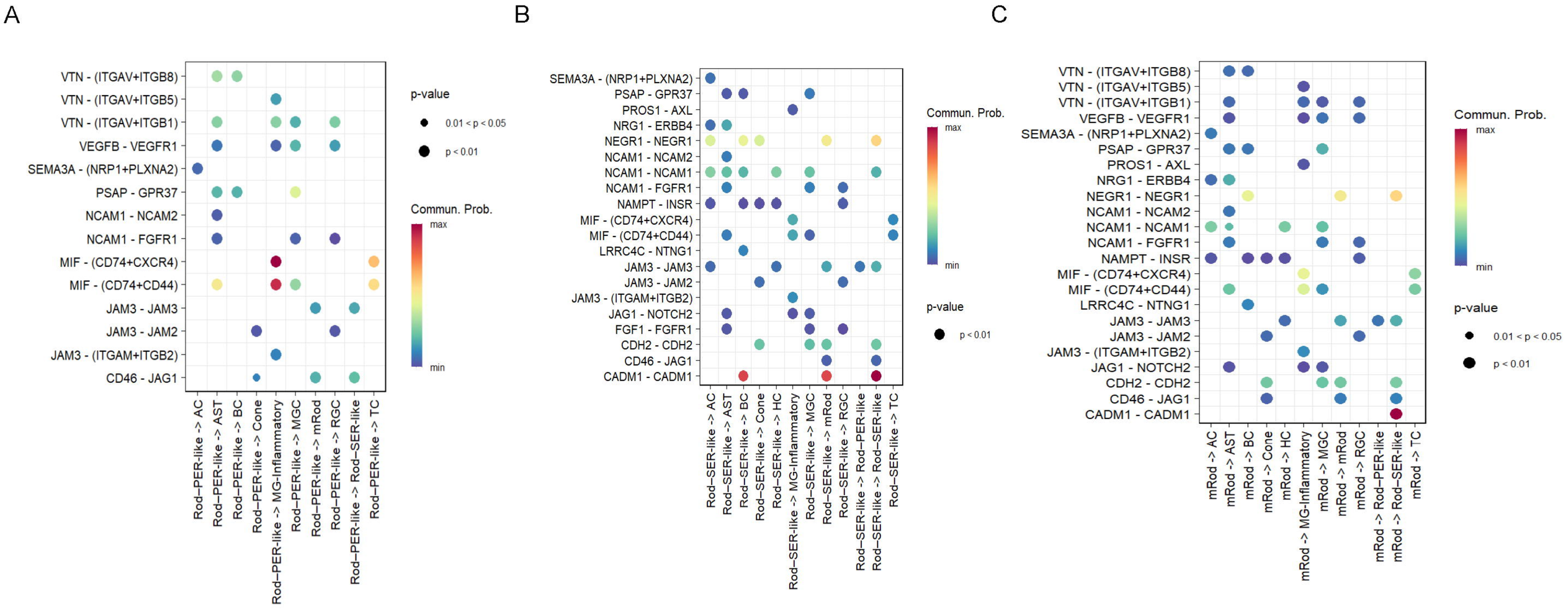
A
VTN - (ITGAV+ITGB8)
VTN - (ITGAV+ITGB5)
VTN - (ITGAV+ITGB1)
VEGFB - VEGFR1
SEMA3A - (NRP1+PLXNA2)
PSAP - GPR37
NCAM1 - NCAM2
NCAM1 - FGFR1
MIF - (CD74+CXCR4)
MIF - (CD74+CD44)
JAM3 - JAM3
JAM3 - JAM2
JAM3 - (ITGAM+ITGB2)
CD46 - JAG1
Rod−PER-like -> AC
Rod−PER-like -> AST
Rod−PER-like -> BC
Rod−PER-like -> Cone
Rod−PER-like -> MG-Inflammatory
Rod−PER-like -> MGC
Rod−PER-like -> mRod
Rod−PER-like -> RGC
Rod−PER-like -> Rod−SER-like
Rod−PER-like -> TC
p-value
0.01 < p < 0.05
p < 0.01
Commun. Prob.
max
min
B
SEMA3A - (NRP1+PLXNA2)
PSAP - GPR37
PROS1 - AXL
NRG1 - ERBB4
NEGR1 - NEGR1
NCAM1 - NCAM2
NCAM1 - NCAM1
NCAM1 - FGFR1
NAMPT - INSR
MIF - (CD74+CXCR4)
MIF - (CD74+CD44)
LRRC4C - NTNG1
JAM3 - JAM3
JAM3 - JAM2
JAM3 - (ITGAM+ITGB2)
JAG1 - NOTCH2
FGF1 - FGFR1
CDH2 - CDH2
CD46 - JAG1
CADM1 - CADM1
Rod−SER-like -> AC
Rod−SER-like -> AST
Rod−SER-like -> BC
Rod−SER-like -> Cone
Rod−SER-like -> HC
Rod−SER-like -> MG-Inflammatory
Rod−SER-like -> MGC
Rod−SER-like -> mRod
Rod−SER-like -> RGC
Rod−SER-like -> Rod−PER-like
Rod−SER-like -> Rod−SER-like
Rod−SER-like -> TC
Commun. Prob.
max
min
p-value
p < 0.01
C
VTN - (ITGAV+ITGB8)
VTN - (ITGAV+ITGB5)
VTN - (ITGAV+ITGB1)
VEGFB - VEGFR1
SEMA3A - (NRP1+PLXNA2)
PSAP - GPR37
PROS1 - AXL
NRG1 - ERBB4
NEGR1 - NEGR1
NCAM1 - NCAM2
NCAM1 - NCAM1
NCAM1 - FGFR1
NAMPT - INSR
MIF - (CD74+CXCR4)
MIF - (CD74+CD44)
LRRC4C - NTNG1
JAM3 - JAM3
JAM3 - JAM2
JAM3 - (ITGAM+ITGB2)
JAG1 - NOTCH2
CDH2 - CDH2
CD46 - JAG1
CADM1 - CADM1
mRod -> AC
mRod -> AST
mRod -> BC
mRod -> Cone
mRod -> HC
mRod -> MG-Inflammatory
mRod -> MGC
mRod -> mRod
mRod -> RGC
mRod -> Rod−PER-like
mRod -> Rod−SER-like
mRod -> TC
Commun. Prob.
max
min
p-value
0.01 < p < 0.05
p < 0.01

A

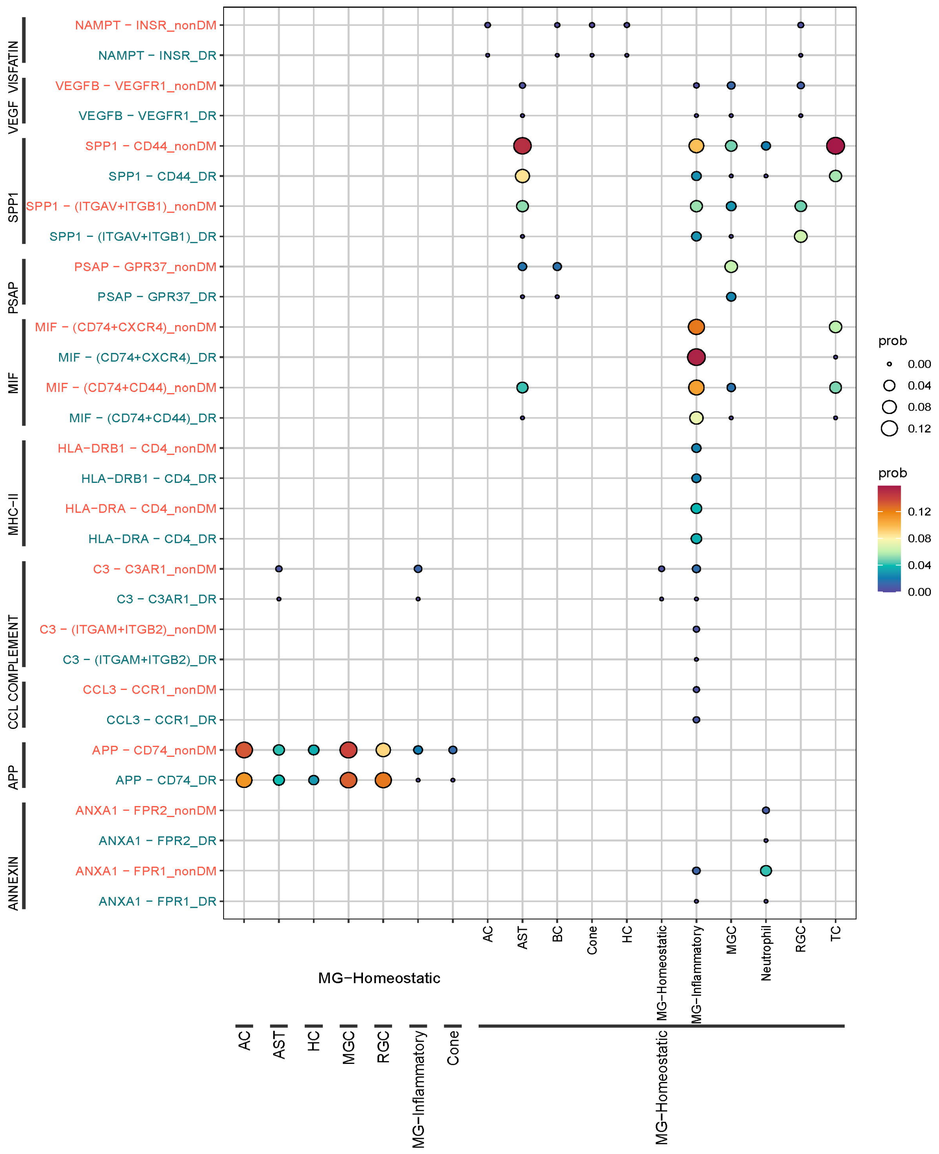
VEGF
VISFATIN
SPP1
PSAP
MIF
MHC−II
COMPLEMENT
CCL
APP
ANNEXIN
NAMPT − INSR_nonDM
NAMPT − INSR_DR
VEGFB − VEGFR1_nonDM
VEGFB − VEGFR1_DR
SPP1 − CD44_nonDM
SPP1 − CD44_DR
SPP1 − (ITGAV+ITGB1)_nonDM
SPP1 − (ITGAV+ITGB1)_DR
PSAP − GPR37_nonDM
PSAP − GPR37_DR
MIF − (CD74+CXCR4)_nonDM
MIF − (CD74+CXCR4)_DR
MIF − (CD74+CD44)_nonDM
MIF − (CD74+CD44)_DR
HLA−DRB1 − CD4_nonDM
HLA−DRB1 − CD4_DR
HLA−DRA − CD4_nonDM
HLA−DRA − CD4_DR
C3 − C3AR1_nonDM
C3 − C3AR1_DR
C3 − (ITGAM+ITGB2)_nonDM
C3 − (ITGAM+ITGB2)_DR
CCL3 − CCR1_nonDM
CCL3 − CCR1_DR
APP − CD74_nonDM
APP − CD74_DR
ANXA1 − FPR2_nonDM
ANXA1 − FPR2_DR
ANXA1 − FPR1_nonDM
ANXA1 − FPR1_DR
prob
0.00
0.04
0.08
0.12
prob
0.12
0.08
0.04
0.00
MG−Homeostatic
AC
AST
BC
Cone
HC
MG−Homeostatic
MG−Inflammatory
MGC
Neutrophil
RGC
TC
AC
AST
HC
MGC
RGC
MG−Inflammatory
Cone
MG−Homeostatic
MG−Inflammatory

B

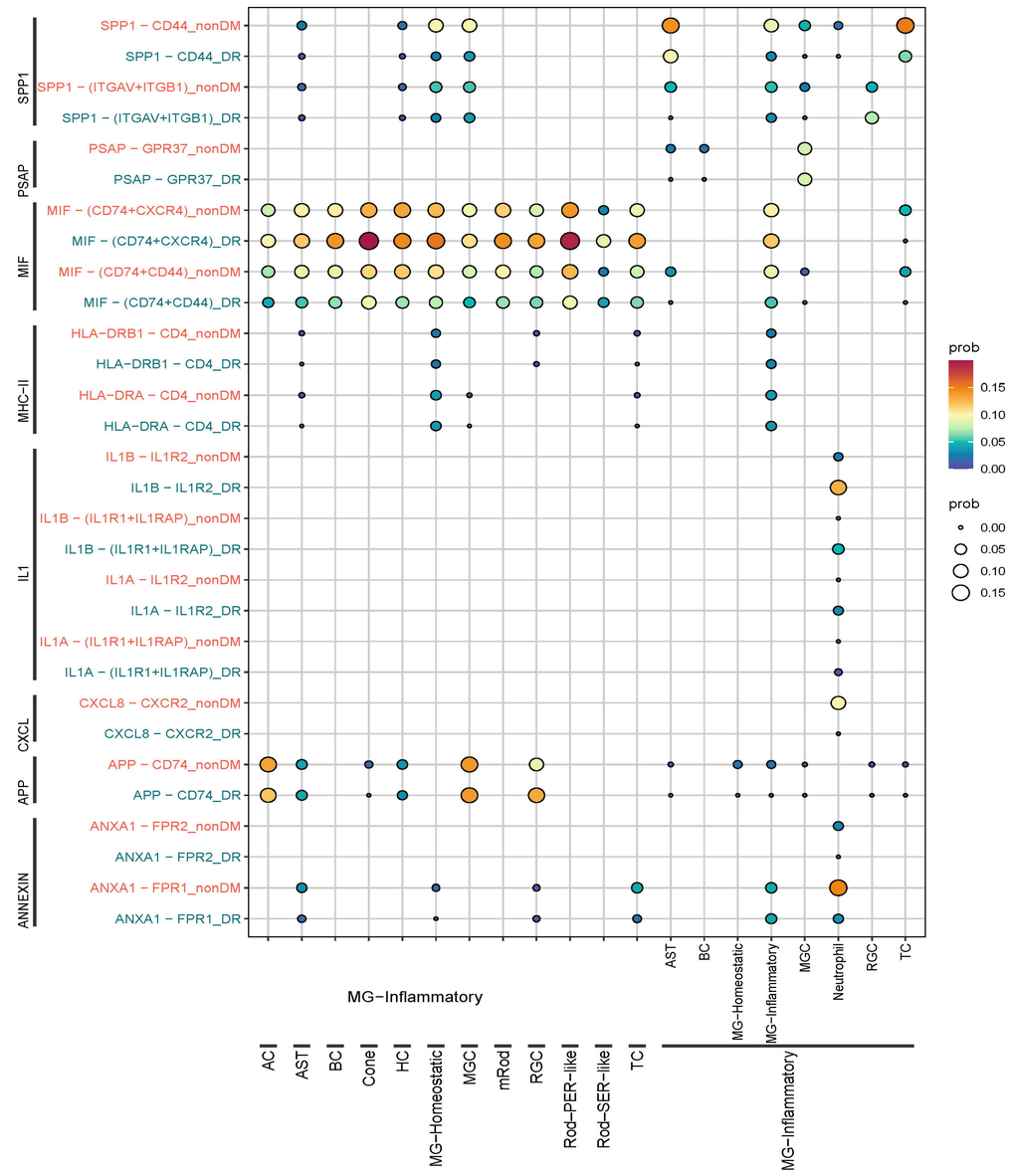
SPP1
PSAP
MIF
MHC−II
IL1
CXCL
APP
ANNEXIN
SPP1 − CD44_nonDM
SPP1 − CD44_DR
SPP1 − (ITGAV+ITGB1)_nonDM
SPP1 − (ITGAV+ITGB1)_DR
PSAP − GPR37_nonDM
PSAP − GPR37_DR
MIF − (CD74+CXCR4)_nonDM
MIF − (CD74+CXCR4)_DR
MIF − (CD74+CD44)_nonDM
MIF − (CD74+CD44)_DR
HLA−DRB1 − CD4_nonDM
HLA−DRB1 − CD4_DR
HLA−DRA − CD4_nonDM
HLA−DRA − CD4_DR
IL1B − IL1R2_nonDM
IL1B − IL1R2_DR
IL1B − (IL1R1+IL1RAP)_nonDM
IL1B − (IL1R1+IL1RAP)_DR
IL1A − IL1R2_nonDM
IL1A − IL1R2_DR
IL1A − (IL1R1+IL1RAP)_nonDM
IL1A − (IL1R1+IL1RAP)_DR
CXCL8 − CXCR2_nonDM
CXCL8 − CXCR2_DR
APP − CD74_nonDM
APP − CD74_DR
ANXA1 − FPR2_nonDM
ANXA1 − FPR2_DR
ANXA1 − FPR1_nonDM
ANXA1 − FPR1_DR
prob
0.15
0.10
0.05
0.00
prob
0.00
0.05
0.10
0.15
MG−Inflammatory
AST
BC
MG−Homeostatic
MG−Inflammatory
MGC
Neutrophil
RGC
TC
AC
AST
BC
Cone
HC
MG−Homeostatic
MGC
mRod
RGC
Rod−PER−like
Rod−SER−like
TC
MG−Inflammatory

C

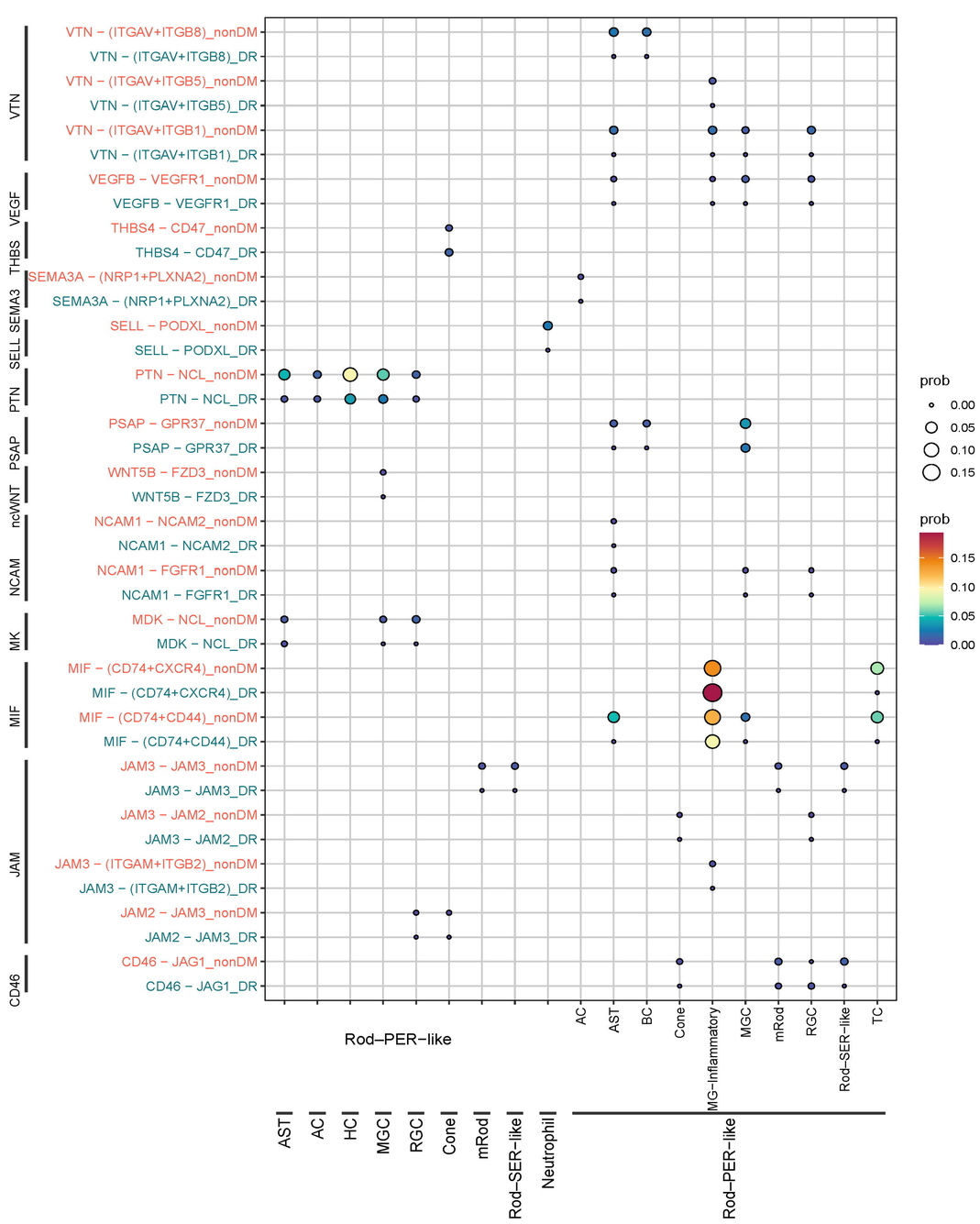
VTN
VEGF
THBS
SEMA3
SELL
PTN
PSAP
ncWNT
NCAM
MK
MIF
JAM
CD46
VTN − (ITGAV+ITGB8)_nonDM
VTN − (ITGAV+ITGB8)_DR
VTN − (ITGAV+ITGB5)_nonDM
VTN − (ITGAV+ITGB5)_DR
VTN − (ITGAV+ITGB1)_nonDM
VTN − (ITGAV+ITGB1)_DR
VEGFB − VEGFR1_nonDM
VEGFB − VEGFR1_DR
THBS4 − CD47_nonDM
THBS4 − CD47_DR
SEMA3A − (NRP1+PLXNA2)_nonDM
SEMA3A − (NRP1+PLXNA2)_DR
SELL − PODXL_nonDM
SELL − PODXL_DR
PTN − NCL_nonDM
PTN − NCL_DR
PSAP − GPR37_nonDM
PSAP − GPR37_DR
WNT5B − FZD3_nonDM
WNT5B − FZD3_DR
NCAM1 − NCAM2_nonDM
NCAM1 − NCAM2_DR
NCAM1 − FGFR1_nonDM
NCAM1 − FGFR1_DR
MDK − NCL_nonDM
MDK − NCL_DR
MIF − (CD74+CXCR4)_nonDM
MIF − (CD74+CXCR4)_DR
MIF − (CD74+CD44)_nonDM
MIF − (CD74+CD44)_DR
JAM3 − JAM3_nonDM
JAM3 − JAM3_DR
JAM3 − JAM2_nonDM
JAM3 − JAM2_DR
JAM3 − (ITGAM+ITGB2)_nonDM
JAM3 − (ITGAM+ITGB2)_DR
JAM2 − JAM3_nonDM
JAM2 − JAM3_DR
CD46 − JAG1_nonDM
CD46 − JAG1_DR
prob
0.00
0.05
0.10
0.15
prob
0.15
0.10
0.05
0.00
Rod−PER−like
AC
AST
BC
Cone
MG−Inflammatory
MGC
mRod
RGC
Rod−SER−like
TC
AST
AC
HC
MGC
RGC
Cone
mRod
Rod−SER−like
Neutrophil
Rod−PER−like

D

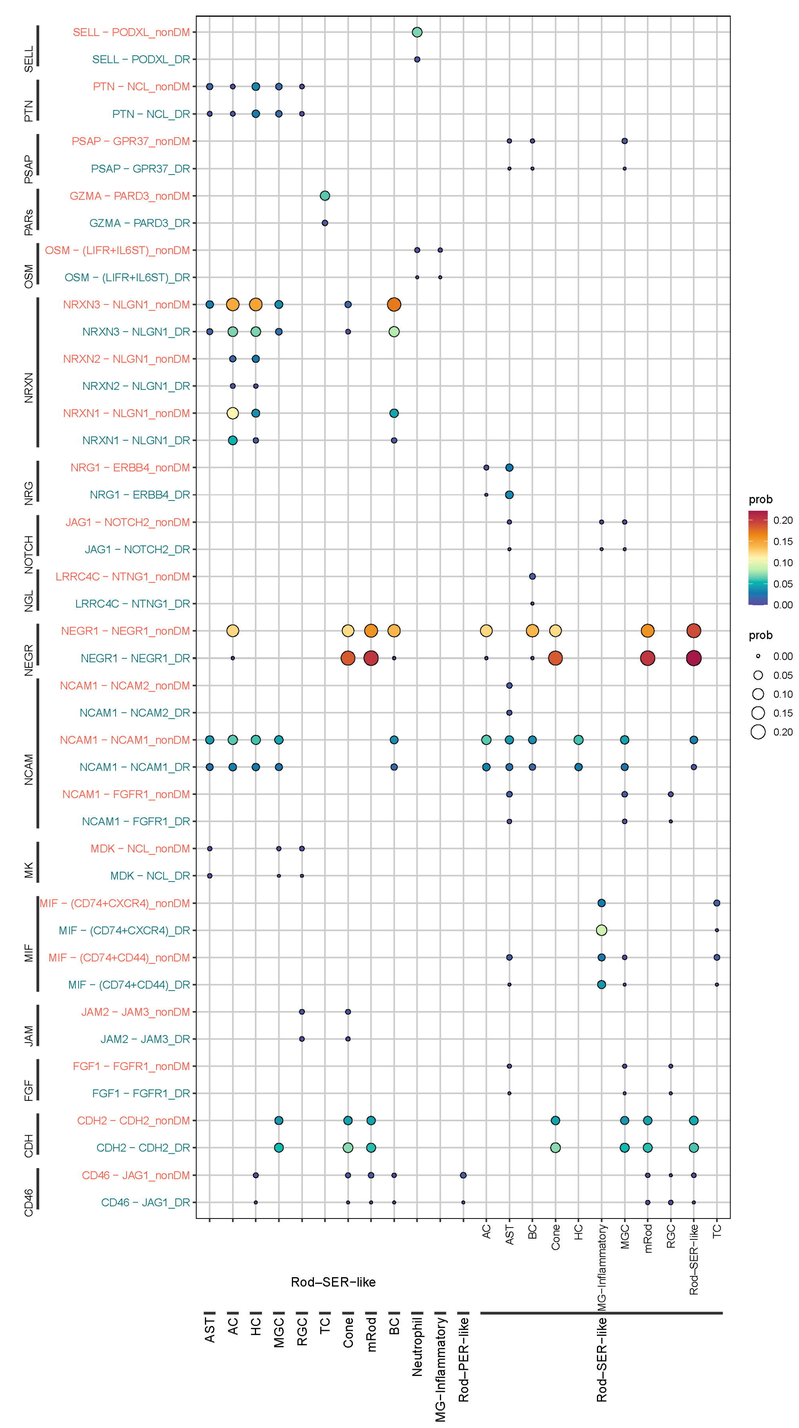
SELL
PTN
PSAP
PARs
OSM
NRXN
NRG
NOTCH
NGL
NEGR
NCAM
MK
MIF
JAM
FGF
CDH
CD46
SELL − PODXL_nonDM
SELL − PODXL_DR
PTN − NCL_nonDM
PTN − NCL_DR
PSAP − GPR37_nonDM
PSAP − GPR37_DR
GZMA − PARD3_nonDM
GZMA − PARD3_DR
OSM − (LIFR+IL6ST)_nonDM
OSM − (LIFR+IL6ST)_DR
NRXN3 − NLGN1_nonDM
NRXN3 − NLGN1_DR
NRXN2 − NLGN1_nonDM
NRXN2 − NLGN1_DR
NRXN1 − NLGN1_nonDM
NRXN1 − NLGN1_DR
NRG1 − ERBB4_nonDM
NRG1 − ERBB4_DR
JAG1 − NOTCH2_nonDM
JAG1 − NOTCH2_DR
LRRC4C − NTNG1_nonDM
LRRC4C − NTNG1_DR
NEGR1 − NEGR1_nonDM
NEGR1 − NEGR1_DR
NCAM1 − NCAM2_nonDM
NCAM1 − NCAM2_DR
NCAM1 − NCAM1_nonDM
NCAM1 − NCAM1_DR
NCAM1 − FGFR1_nonDM
NCAM1 − FGFR1_DR
MDK − NCL_nonDM
MDK − NCL_DR
MIF − (CD74+CXCR4)_nonDM
MIF − (CD74+CXCR4)_DR
MIF − (CD74+CD44)_nonDM
MIF − (CD74+CD44)_DR
JAM2 − JAM3_nonDM
JAM2 − JAM3_DR
FGF1 − FGFR1_nonDM
FGF1 − FGFR1_DR
CDH2 − CDH2_nonDM
CDH2 − CDH2_DR
CD46 − JAG1_nonDM
CD46 − JAG1_DR
prob
0.20
0.15
0.10
0.05
0.00
prob
0.00
0.05
0.10
0.15
0.20
Rod−SER−like
AC
AST
BC
Cone
HC
MG−Inflammatory
MGC
mRod
RGC
Rod−SER−like
TC
AST
AC
HC
MGC
RGC
TC
Cone
mRod
BC
Neutrophil
MG−Inflammatory
Rod−PER−like
Rod−SER−like